Title

Realizing continuous cation order-to-disorder tuning in a class of high-energy spinel-type Li-ion cathodes

Journal

Matter, 4(12)

ISSN

2590-2393

Authors

Cai, Zijian

Ji, Huiwen

Ha, Yang

et al.

Publication Date

2021-12-01

DOI

10.1016/j.matt.2021.10.013

Realizing continuous cation order-to-disorder tuning in a class of high-energy spinel-type Li-ion cathodes

Zijian Cai[1,2], Huiwen Ji[3,11*], Yang Ha[5], Jue Liu[6], Deok-Hwang Kwon[1,2], Yaqian Zhang[1], Alexander Urban[7], Emily E. Foley[8,9], Raynald Giovine[8,9], Hyunchul Kim[2], Zhengyan Lun[1,2], Tzu-Yang Huang[3,4], Guobo Zeng[1,2], Yu Chen[1,2], Jingyang Wang[1,2], Bryan D. McCloskey[3,4], Mahalingam Balasubramanian[10], Raphaële J. Clément[8,9], Wanli Yang[5], Gerbrand Ceder[1,2,*†]

[1] *Department of Materials Science and Engineering, University of California Berkeley, Berkeley, CA 94720, USA*

[2] *Materials Sciences Division, Lawrence Berkeley National Laboratory, Berkeley, CA 94720, USA*

[3] *Energy Storage and Distributed Resources Division, Lawrence Berkeley National Laboratory, Berkeley, CA, USA.*

[4] *Department of Chemical and Biomolecular Engineering, University of California Berkeley, Berkeley, CA 94720, USA*

[5] *The Advanced Light Source, Lawrence Berkeley National Laboratory, Berkeley, CA, USA*

[6] *Neutron Scattering Division, Oak Ridge National Laboratory, Oak Ridge, TN, USA*

[7] *Department of Chemical Engineering, Columbia University, New York, NY, USA*

[8] *Materials Department, University of California Santa Barbara, Santa Barbara, CA 93106, USA*

[9] *Materials Research Laboratory, University of California Santa Barbara, CA 93106-5121, USA.*

[10] *X-Ray Science Division, Advanced Photon Source, Argonne National Laboratory Argonne, IL 60439, USA*

[11] *Department of Materials Science and Engineering, Univeristy of Utah, Salt Lake City, UT 84112, USA*

[*]Corresponding author: Huiwen Ji (huiwen.ji@utah.edu), Gerbrand Ceder (gceder@berkeley.edu)

)

Summary

Conventional Li-ion cathode materials are dominated by well-ordered structures, in which Li and transition metals (TM) occupy distinct crystallographic sites. We show in this paper that profoundly new degrees of freedom for the optimization of electrochemical properties may be accessed if controllable cation disorder is introduced. In a class of high-capacity spinel-type cathode materials, we identify cation to anion ratio in synthesis as a key parameter for tuning the structure continuously from a well-ordered spinel, through a partially ordered spinel, to rocksalt. We find that the varying degree of cation disorder modifies the voltage profile, rate capability and charge-compensation mechanism in a rational and predictable way. Our results indicate that spinel-type order is most beneficial for achieving high rate performance as long as the cooperative 8a to 16c phase transition is suppressed, while more rocksalt-like disorder facilitates O redox which can increase capacity. Our findings reveal an important tuning handle for achieving high energy and power in the vast space of partially ordered cathode materials.

Introduction

Lithium-ion (Li-ion) batteries are the ubiquitous energy storage solution for portable electronics in our modern society. Over the next decade, the demand for Li-ion technology is projected to further grow more than tenfold,[1] largely driven by the electrification of transportation. Meanwhile, several other market segments that are still in their early stage of development, including residential and grid-scale storage, may further open up if battery costs continue to drop. The rapid scale-up in Li-ion production brings new challenges of supply and resource sustainability, especially for cobalt and nickel, which are the two major components for cathode fabrication.[1] Most of the conventional cathode materials, including $LiCoO_2$ and $Li(Ni,Co,Mn)O_2$ (NMC), are based on a layered crystal structure, in which Li and TM form alternating layers to enable facile Li transport in a 2D open space. This layered structure necessitates the use of Ni and Co as redox active elements, as other transition metals migrate into the Li layer in either their oxidized or reduced state.[2] To ensure energy security and alleviate supply chain risks, the structural and chemical diversity of cathode compounds needs to be broadened. In this work, we show that considerable opportunity exists in the continuum between well-ordered spinels and disordered rocksalts.

Spinel exhibits the same anion (oxygen) sublattice as the layered structure but a different cation order. In a perfectly ordered spinel $LiTM_2O_4$, Li and TM occupy the tetrahedral 8a and octahedral 16d sites, respectively. The structure is advantageous for transport as Li ions can diffuse in local channels that do not face-share with TM ions[3] and interconnect to form a 3D percolating network. However, for the most common spinel cathode, $LiMn_2O_4$, only half of the potential Li capacity can be practically utilized due to a first-order phase transition that occurs near 3 V (versus Li^+/Li) once the compound is lithiated beyond the $LiMn_2O_4$ composition. This

phase transition, coupled with the Jahn-Teller distortion of Mn^{3+}, leads to poor kinetics and poor cyclability.

Converting the two-phase regions into a continuous solid solution is expected to reduce capacity loss (due to the reduction of strain upon cycling) and improve kinetics. Past efforts have focused on partial substitution of Jahn-Teller-inactive elements for Mn^{3+} in the 16d site, keeping the 8a fully occupied by Li. For example, substituting Ni^{2+} for Mn^{3+} results in partial or complete TM mixing in the 16d site and converts the 4 V plateau into a solid-solution region.[4] Yet the two-phase region near 3 V is retained.[5] Substituting Li^{+} for Mn^{3+} is more efficient in tuning the reaction thermodynamics. Previous operando neutron studies indicated that $Li_{1.1}Mn_{1.9}O_4$, with 5% Li-for-Mn substitution undergoes a pure solid-solution reaction at the 4 V plateau,[6] unlike $LiMn_2O_4$. Further increasing Li substitution leads to the Li-rich limiting composition $Li_4Mn_5O_{12}$, which can be cycled between $Li_2Mn_5O_{12}$ and $Li_{6.5}Mn_5O_{12}$ with some capacity coming from oxygen redox.[7] Nevertheless, the two-phase behavior still appears when the Mn valence drops below 3.5.[8] Recently, it has been demonstrated that ultrahigh energy and power density can be achieved in a class of partially-(dis)ordered Li-Mn-O-F spinels with as much as 20% Li-for-Mn substitution and significant cation over-stoichiometry.[9] Fluorination is applied to reduce the overall Mn valence, thereby increasing the theoretical transition metal capacity. Previous work has also demonstrated that fluorination mitigates irreversible oxygen loss and increase average Li insertion/extraction voltage.[10-14] Fluorination and Li-for-Mn substitution also separates the composition where all octahedral sites are filled from the composition where all Mn^{3+} is Jahn-Teller active, limiting the way in which these two effects strengthen the two-phase reaction in $LiMn_2O_4$. The materials presented in this work exhibit cation disorder that is no longer confined to the 16d site but also involves the 8a and 16c sites. Since the two-phase reaction at ~ 3 V upon

lithiation for a classic well-ordered $LiMn_2O_4$ cathode originates from a collective migration of Li from the 8a site to the 16c site, the partial cation (transition metal) disorder introduced between the 16d and the 16c sites is expected to reduce this collective behavior and possibly convert the two-phase reaction into a solid-solution reaction. Indeed, nearly smooth voltage profiles are observed in the materials we tested, indicating the absence of two-phase regions, along with exceptionally high capacity and energy density. The discovery opens up the vast space between the perfectly ordered spinel and the fully cation-disordered end member. To facilitate rational cathode design in this space, it is desirable to identify the chemical and structural variables that control the degree of order and understand their impact on performance.

In this study, we successfully synthesized the $Li_{1.4+x}Mn_{1.6}O_{3.7}F_{0.3}$ compositional series ($0.07 < x < 1$) using a mechanochemical method. These materials exhibit much higher capacity (> 350 mAh g^{-1}) and energy density (> 1,000 Wh kg^{-1}) than the prototype $LiMn_2O_4$ obtained under the same synthesis conditions. We find that the Li over-stoichiometry content x introduced during synthesis is a useful handle for tuning the degree of cation disorder. As x increases, the structure evolves from spinel-like cation order to almost complete cation disorder. Accordingly, the electrochemical voltage profile becomes more sloping in the 3 V region. The modified cation order also affects the Li transport kinetics and redox mechanism, which our computational analysis attributes to the modified short-range and long-range structural order.

Results

Design, synthesis and structural characterizations

To obtain spinel-type cathodes with a large practical capacity, we follow the design rules depicted in Figure 1. A fully ordered spinel has well-percolating Li diffusion channels (Figure 1a and 1b(left)) but suffers from a kinetically-slow and structurally destructive two-phase reaction associated with the collective Li 8a-to-16c transition when $LiMn_2O_4$ is lithiated to $Li_2Mn_2O_4$. A three-pronged strategies is employed to suppress or reduce the two-phase region, represented by a general stoichiometry of $Li_{1+x+y}Mn_{2-y}(O,F)_4$: 1) Substitution of some Mn on the 16d site to facilitate Mn/Li disorder and facilitate the incorporation of excess Li; 2) Introduction of extra Li (x >0) to occupy some of the previously empty 16c sites and create some face sharing Li_{tet}-Li_{oct} which are believed to create fast Li-ion transport pathways in spinel-like materials;[15] 3) Creation of Mn disorder among the 16c/16d sites by ball milling to reduce the spinel-like order. We selected a 20% Li substitution on 16d site (y = 0.4 in $Li_{1+x+y}Mn_{2-y}(O,F)_4$) based on previous percolation analysis and focus on the tuning of x in this study.

Three partially-(dis)ordered spinels $Li_{1.47}Mn_{1.6}O_{3.7}F_{0.3}$ (0.07 excess cations per spinel formula unit) , $Li_{1.68}Mn_{1.6}O_{3.7}F_{0.3}$ (0.28 excess cations) and $Li_2Mn_{1.6}O_{3.7}F_{0.3}$ (0.6 excess cations) were synthesized by a mechanochemical ball-milling method. Fluorination was used to charge-compensate the Li substitution, increase the TM capacity by lowering the Mn valence, and improve cyclability.[10,11,16] Synchrotron X-ray diffraction (SXRD) patterns in Figure 2a indicate that the three compounds can be indexed to a single-phase spinel structure with various degrees of cation disorder. After normalizing the intensity of each SXRD pattern by that of the corresponding (400) peak, we observe a weakening (111) diffraction peak at a d spacing between 4 and 5 Å as the Li over-stoichiometry x increases from 0.07 to 0.6. This result, according to

Rietveld refinement, indicates that Li over-stoichiometry creates Mn disorder between the 16c and 16d sites. To obtain the Li occupancies, neutron diffraction (ND), which is sensitive to light elements, was conducted. The Mn site occupancies are obtained from refinement of the SXRD pattern (Table S2-4) and fixed when refining the ND data. The final cation occupancies in the 8a, 16c and 16d sites are summarized in Table 1. Other refinement details can be found in Tables S1–4. This combined neutron/synchrotron XRD indicates that as the Li over-stoichiometry is increased the structure evolves from being mostly spinel-like-ordered, towards a hybrid spinel-rocksalt type of disorder with more cations on the octahedral site. All evidence indicates that this is a single-phase structure and not a composite of a spinel and rocksalt structure.

Scanning electron microscopy (SEM) was applied to characterize the particle morphology. We do not include the characterization of $Li_{1.68}Mn_{1.6}O_{3.7}F_{0.3}$ as it was reported in previous work.[9] As shown in Figure 3a–b, $Li_{1.47}Mn_{1.6}O_{3.7}F_{0.3}$ and $Li_2Mn_{1.6}O_{3.7}F_{0.3}$ have a primary particle size of 100–200 nm post mechanochemical synthesis, which is comparable to that in $Li_{1.68}Mn_{1.6}O_{3.7}F_{0.3}$.[9] In the lower-magnification SEM images, agglomeration of primary particles into secondary particles was observed (Fig. S4). To verify the compositional homogeneity, scanning transmission electron microscopy (STEM) and energy dispersion spectroscopy (EDS) mapping were performed and the results are presented in Figure 3c–d. All the detectable elements, Mn, O, and F, are uniformly distributed in $Li_{1.47}Mn_{1.6}O_{3.7}F_{0.3}$ and $Li_2Mn_{1.6}O_{3.7}F_{0.3}$. To verify whether the structure is a single-phase partially-(dis)ordered spinel, high-resolution transmission electron microscopy (HRTEM) and electron diffraction (ED) were performed. The characteristic *d* spacing of ~ 4.8 Å, which corresponds to the spinel (111) planes, is marked by white lines in the HRTEM images (Figure 3e, f). The ED patterns of both $Li_{1.47}Mn_{1.6}O_{3.7}F_{0.3}$ and $Li_2Mn_{1.6}O_{3.7}F_{0.3}$ can be indexed to a spinel crystal structure.

^{19}F and ^{7}Li solid-state nuclear magnetic resonance (ssNMR) measurements were conducted to further verify the integration of F in the bulk structure (Figure 4). The spectra obtained on the $Li_{1.47}Mn_{1.6}O_{3.7}F_{0.3}$ and $Li_2Mn_{1.6}O_{3.7}F_{0.3}$ pristine powders show two distinct components: a broad, paramagnetic signal and a sharp, diamagnetic signal. The broad signal corresponds to ^{19}F nuclei in the bulk of the cathode materials. Their interaction with nearby paramagnetic Mn ions leads to a shift of the ^{19}F resonant frequency away from that of diamagnetic LiF at −204 ppm and to significant spectral broadening. Additionally, for both compounds, the observed paramagnetic lineshape comprises several broad and overlapping ^{19}F signals assigned to a wide variety of ^{19}F local environments in the partially-(dis)ordered spinel lattice. The sharp signal centered at −204 ppm is assigned to a diamagnetic LiF impurity phase present in small amounts in these two samples. We note that NMR signals from ^{19}F nuclei directly bonded to paramagnetic Mn species in the bulk cathode materials are too broad (and short-lived) to be observed experimentally, which prevents the exact quantification of the LiF impurity phase in these samples. If anything, the amount of LiF impurity phase obtained from ^{19}F NMR data is overestimated, indicating that the majority of F ions are incorporated into the bulk of the partially disordered spinel compounds.

The integration on quantitative ^{7}Li spin echo spectra was performed to further characterize the Li local environments. By integrating the sharp signal close to 0 ppm in each spectra the fraction of Li present in diamagnetic environments (*e.g.* in Li_2CO_3, Li_2O, or LiF) was found to be 2% and 1% (+/− 1%) for $Li_{1.47}Mn_{1.6}O_{3.7}F_{0.3}$ and $Li_2Mn_{1.6}O_{3.7}F_{0.3}$, respectively. This intensity provides the upper limit for the amount of impurity phases present in the samples, as the signal could also arise from the formation of large diamagnetic Li-rich (Mn-poor) domains within the disordered oxide matrix.[17] Overall, the fraction of diamagnetic ^{7}Li environments in these disordered spinel

samples is no more than 3% of the total Li content, we conclude that there is excellent F solubility in the $Li_{1.47}Mn_{1.6}O_{3.7}F_{0.3}$ and $Li_2Mn_{1.6}O_{3.7}F_{0.3}$ spinel compositions.

Voltage profiles modified by structural order

The three partially (dis)ordered spinels $Li_{1.4+x}Mn_{1.6}O_{3.7}F_{0.3}$ (x = 0.07, 0.28, and 0.6) exhibit distinct voltage profiles. As shown in Figure 5a, both the small voltage step near 4 V and the plateau-like feature near 3 V gradually disappear as x increases from 0.07 to 0.6, leading to a smoother and more sloping profile. Such variation is better captured by the dQ/dV curves shown in Figure 5b. In a perfectly-ordered $LiMn_2O_4$ spinel, the 3V plateau upon lithiation is associated with the collective 8a-to-16c O transition resulting in a two-phase reaction between a cubic phase and a tetragonal phase.[18] Our voltage curves show no true plateau region anymore in $Li_{1.47}Mn_{1.6}O_{3.7}F_{0.3}$ and the pseudo plateau near 3V is significantly narrower than that in ordered spinel, suggesting suppression of the two-phase reaction. As more cation disorder is introduced with the $Li_2Mn_{1.6}O_{3.7}F_{0.3}$ composition, the pseudo plateau disappears. Instead, more Li is extracted or inserted between 3.1 and 3.7 V. As a result, the average voltage as calculated from the first discharge process slightly increases from 2.99 V for x = 0.07 to 3.08 V for x = 0.6. There is no discernible voltage plateau near 4 V, likely due to the partial occupancy of the octahedral 16c sites, which reduces the tetrahedral Li occupation in the face-sharing 8a sites.

The room-temperature galvanostatic cycling performance is shown in Figure 6a–c. In the three cathode materials, the amount of available Li capacity is the same, which equals 2.4 Li per f.u. between the two limiting compositions of $Mn_{1.6}O_{3.7}F_{0.3}$ and $Li_{2.4}Mn_{1.6}O_{3.7}F_{0.3}$. Therefore, when cycled in a wide voltage range between 1.5 and 4.8 V, all three cathode materials exhibit comparably high gravimetric capacity > 350 mAh g^{-1} and energy density > 1,000 Wh kg^{-1}. But more capacity and energy is delivered at high voltages for the materials with a higher initial Li over-stoichiometry level. $Li_2Mn_{1.6}O_{3.7}F_{0.3}$ delivers a capacity of 226 mAh g^{-1} (813 Wh kg^{-1}) above 3 V, which decreases to 201 mAh g^{-1} (726 Wh kg^{-1}) for $Li_{1.68}Mn_{1.6}O_{3.7}F_{0.3}$ and 163 mAh

g^{-1} (598 Wh kg^{-1}) for $Li_{1.47}Mn_{1.6}O_{3.7}F_{0.3}$. To measure the long-term stability, the three cathode materials were cycled at 50 mA g^{-1} in the 1.5–4.8 V (red squares) and 2.0–4.4 V (blue circles) ranges for 30 continuous cycles. The results are shown in Figure 5d–f. $Li_{1.47}Mn_{1.6}O_{3.7}F_{0.3}$ shows better capacity retention than the more Li-over-stoichiometric $Li_{1.68}Mn_{1.6}O_{3.7}F_{0.3}$ and $Li_2Mn_{1.6}O_{3.7}F_{0.3}$, in the 1.5–4.8 V range. To characterize any irreversible oxygen release and its relations to capacity loss, differential electrochemical mass spectrometry (DEMS) was performed on two representative compositions, $Li_{1.47}Mn_{1.6}O_{3.7}F_{0.3}$ and $Li_2Mn_{1.6}O_{3.7}F_{0.3}$. Both compounds showed minimal oxygen loss with $Li_2Mn_{1.6}O_{3.7}F_{0.3}$ showing the higher oxygen loss. The results correlate with the observation of slightly less capacity retention between 1.5-4.8V for the more cation-disordered $Li_2Mn_{1.6}O_{3.7}F_{0.3}$ than for the more ordered $Li_{1.47}Mn_{1.6}O_{3.7}F_{0.3}$, indicating that unstable oxygen redox and oxygen loss at high voltage might be one origin of the capacity degradation. In a narrower voltage window of 2.0–4.4 V, $Li_{1.47}Mn_{1.6}O_{3.7}F_{0.3}$, $Li_{1.68}Mn_{1.6}O_{3.7}F_{0.3}$ and $Li_2Mn_{1.6}O_{3.7}F_{0.3}$ show enhanced capacity retention of 90.7%, 88.7% and 93.8%, respectively, after 30 cycles, with an initial capacity of ~200 mAh g^{-1}.

Rate capability

Modifying the cation order is expected to directly alter the local atomic arrangement and the percolation of Li migration channels in the structure,[3] which both dictate the Li transport properties. We therefore investigated the rate capability of the three spinel oxyfluorides with various degrees of cation disorder, at current densities from 100 to 7,500 mA g^{-1}. A baseline material $LiMn_2O_4$ and a completely cation-disordered rocksalt (also known as DRX) $Li_{2.4}Mn_{1.6}O_{3.7}F_{0.3}$, synthesized by the same mechanochemical method, are included for comparison. Similar Li-Mn-O-F DRXs have been extensively studied and reported before.[19] The XRD pattern of the as-synthesized $LiMn_2O_4$ can be indexed to a cubic spinel structure (Figure S12a). When cycled at a low current density of 50 mA g^{-1}, the voltage profile of the material exhibits the 3 V and 4 V plateaus characteristic of the octahedral and tetrahedral Li insertion/extraction in a classic $LiMn_2O_4$ spinel cathode (Figure S12). Each rate test was done on a fresh cell and the voltage profiles of the second cycles at the given rates are shown in Figure 7a. The rate performance of the series is compared in a Ragone plot in Figure 7b.

All four Li-Mn oxyfluorides with various initial Li over-stoichiometry show better rate capability than the baseline $LiMn_2O_4$. In $LiMn_2O_4$, a voltage plateau at ~2.8 V is observed at low rate, but this plateau shrinks at higher rates. Previously, ultrahigh rate capability was demonstrated in $Li_{1.68}Mn_{1.6}O_{3.7}F_{0.3}$ at up to 20 A g^{-1} using a high carbon loading of 50 wt%.[9] In this work, we kept a cathode formulation of 70:20:10 (wt%) active material, carbon black and Teflon. We found that while $Li_{1.68}Mn_{1.6}O_{3.7}F_{0.3}$ delivers the highest capacity at 100 mA g^{-1}, $Li_{1.47}Mn_{1.6}O_{3.7}O_{0.3}$ shows better rate capability by providing the highest capacity at 2,000 mA g^{-1}. $Li_{1.47}Mn_{1.6}O_{3.7}O_{0.3}$ retains a capacity of 158 mAh g^{-1} at 7,500 mA g^{-1}, corresponding to ~48% of

the capacity at 100 mA g^{-1}. In addition, as the Li over-stoichiometry increases from 0.07 to 1.0 in the four Li-Mn oxyfluorides, a decrease in rate capability is observed.

Redox mechanism

The extraction or insertion of Li ions is accompanied by local charge compensation, the mechanism of which alters with variations in structural and chemical order. To probe the detailed redox mechanism, *in-situ* hard X-ray absorption spectroscopy (XAS) and *ex-situ* soft X-ray mappings of resonant inelastic X-ray scattering (mRIXS) measurements were carried out. We selected $Li_{1.47}Mn_{1.6}O_{3.7}F_{0.3}$ and $Li_2Mn_{1.6}O_{3.7}F_{0.3}$ as two representative compositions with a low and high Li over-stoichiometry level.

The X-ray absorption near-edge structure (XANES) is ideal for tracking the Mn valence change in operando because of its excellent bulk sensitivity and short data collection time. Figure 8a–b shows the Mn *K*-edge XANES spectra of $Li_{1.47}Mn_{1.6}O_{3.7}F_{0.3}$ and $Li_2Mn_{1.6}O_{3.7}F_{0.3}$ at selected states of charge during operando cycling. The complete operando spectra are shown in the Figure S5-7. By comparing their edge positions with those of the references (MnO, Mn_2O_3 and MnO_2), the Mn valence at various states of charge (SOC) can be estimated. In the pristine sample Mn is between 3+ and 4+ and is slightly higher in $Li_{1.47}Mn_{1.6}O_{3.7}F_{0.3}$ than in $Li_2Mn_{1.6}O_{3.7}F_{0.3}$. The observation agrees with our expectation of $Mn^{3.89+}$ in $Li_{1.47}Mn_{1.6}O_{3.7}F_{0.3}$ and $Mn^{3.56+}$ in $Li_2Mn_{1.6}O_{3.7}F_{0.3}$ deduced from the composition. During the first charge, Mn in both samples is oxidized to approximately Mn^{4+}, while upon discharge, the edge positions reverse to an energy between that in Mn_3O_4 and Mn_2O_3. During the second charge, the Mn *K*-edge reversibly shifts again to a position close to that of 4+, indicating a reversible Mn redox process. However, the main edge of XANES spectra cannot be used to precisely quantify the oxidation state because it measures dipole transitions from 1*s* to 4*p* orbitals, which do not involve the 3*d* valence states.

We also utilized *ex-situ* mRIXS at the Mn *L*-edge to quantify the evolution of Mn valences upon cycling. The technique directly probes the excitation from Mn 2*p* core states to 3*d* valence states.

The Mn *L*-edge spectra can be obtained from the inverse partial fluorescence yield (iPFY) signal of the Mn RIXS map, which is a non-distorted bulk probe of the Mn 3*d* states.[20-22] The quantification was done by fitting the experimental L_3-edge as a linear combination of $Mn^{2+/3+/4+}$ reference spectra to generate the Mn valences (Figure 8c-d). The results are plotted in Figure 8e–f together with the electrochemical profile. The Mn valence in the pristine state is 3.75+ for $Li_{1.47}Mn_{1.6}O_{3.7}F_{0.3}$ and 3.56+ for $Li_2Mn_{1.6}O_{3.7}F_{0.3}$. Note that the actual pristine Mn states can be slightly lower than theoretical value due to the inert atmosphere used in synthesis, and the deviation is usually more significant for compounds with a higher Mn valence.[9] The Mn valence in the two materials increases to ~3.84+ when charged to 4.5 V and slightly dropped when further charged to 4.8 V, a phenomenon that has been previously observed and is associated with the complex interplay between O and TM oxidation processes at the top of charge.[23,24] At the beginning of discharge, the Mn valence remains constant until 3.6 V, suggesting the dominance of O reduction in this region. Once passed 3.6 V, the Mn valence decreases almost linearly and therefore the capacity in this region is contributed mainly by Mn reduction. At the bottom of discharge, the Mn valence is determined to be 2.89+ for $Li_{1.47}Mn_{1.6}O_{3.7}F_{0.3}$ and 3.05+ for $Li_2Mn_{1.6}O_{3.7}F_{0.3}$. Based on the characterized Mn valence change during discharge, the Mn reduction process contributes 1.48 e^-/f.u. to the observed 2.13 Li/f.u. capacity for $Li_{1.47}Mn_{1.6}O_{3.7}F_{0.3}$ (and 1.16 e^-/f.u. to the observed 2.20 Li/f.u. capacity for $Li_2Mn_{1.6}O_{3.7}F_{0.3}$). The discrepancy between the TM and overall capacity points to the participation of O redox.[25]

To more directly examine the contribution from anionic redox, mRIXS measurements at the O *K*-edge were conducted. Previous studies have established that a characteristic feature at 523.7 eV emission energy and 531.0 eV excitation energy is a fingerprint of bulk O oxidation.[20,25,26] We therefore mapped the RIXS signal in the vicinity of this region for a series of SOCs during

the first cycle for $Li_{1.47}Mn_{1.6}O_{3.7}F_{0.3}$ and $Li_2Mn_{1.6}O_{3.7}F_{0.3}$. The results are shown in Figure 9a. In both compounds, the characteristic feature (highlighted by red arrows) is already present at 4.5 V and becomes stronger at 4.8 V (full mapping in Figure S8). During discharge, the feature reversibly fades and vanishes at 1.5 V. The two compounds with a different degree of cation disorder show different intensity of oxidized O at the same SOC, which is manifested in the RIXS cuts of O *K*-edge at the 531.0 eV excitation energy in Figure 9b. The black dashed line at 523.7 eV highlights the emission energy at which the oxidized O signal is expected to appear. At 4.5 V, $Li_2Mn_{1.6}O_{3.7}F_{0.3}$ shows a more intense oxidized O peak than $Li_{1.47}Mn_{1.6}O_{3.7}F_{0.3}$, indicating more O oxidation. The feature is also noticeably stronger for $Li_2Mn_{1.6}O_{3.7}F_{0.3}$ when further charged to 4.8 V and later discharged to 3.6 V. After vanishing at the end of discharge, the signal reappears when charged the second time to 4.8 V (Figure 9a) and shows a similar lineshape to that of 1C4.8V (Figure 9b), suggesting the reversible nature of the O redox processes.

Discussion

Our work shows the remarkable potential of optimizing electrochemical performance by tuning cation disorder. In this work, we show three partially-(dis)ordered spinel compounds with high specific capacity, over 350 mAh g^{-1}, and specific energy over 1,000 Wh kg^{-1}. Among the three, $Li_{1.68}Mn_{1.6}O_{3.7}F_{0.3}$ was reported as an ultrahigh-power-density cathode in our previous work.[9] Here, by carefully tuning the cation disorder level, we find that $Li_{1.47}Mn_{1.6}O_{3.7}F_{0.3}$ delivers a superior specific energy compared to $Li_{1.68}Mn_{1.6}O_{3.7}F_{0.3}$ (Figure 7b) and many other state-of-the-art Li-ion cathodes.[9] While previous cathode discovery has focused on well-ordered compounds,[27,28] and more recently on cation-disordered compounds,[13,29-31] the current work shows the benefits of exploring the large space of partially ordered structures, where cation ordering, in addition to crystal structure, can be used as a design handle. By creating three compositions with increasing cation/anion ratio we bridge the gap between stoichiometric spinels (having a 3 to 4 cation/anion ratio) and rocksalts (with a 1 to 1 cation/anion ratio). While spinels are expected to have the highest intrinsic Li mobility due to their remarkable percolation of Li diffusion channels with low migration energy,[3] the presence of the first order transition that displaces lithium from the 8a to 16c site is an extrinsic barrier to high rate charging, and furthermore leads to mechanically induced capacity degradation. These insights explain why remaining close to the spinel composition but introducing enough cation over-stoichiometry to remove the two-phase region, as in the $Li_{1.47}Mn_{1.6}O_{3.7}F_{0.3}$ composition, leads to the highest rate capability.

The three compounds evaluated here have the same Mn/anion and O/F ratio but only differ by their Li content in the synthesis. This difference may not appear important as the Li content will be changed upon electrochemical cycling, but our results indicate that the over-stoichiometry of

cations (regulated by the amount of lithium) is needed to control the amount of Mn 16c/16d disorder in the synthesis. When the cation excess is low, more spinel-like material is obtained as evidenced by the stronger (111) reflection in the XRD (Figure 2), while a higher Li content brings the material closer to the rocksalt structure.

As we show in this work, tuning the degree of cation order alters the voltage profile, the rate capability, and the amount of oxygen redox (and hence the cycling stability). The voltage profile changes because the Gibbs free energy E as a function of Li content x_{Li} is modified by cation (dis)order and so is the voltage profile $\sim\frac{\delta E(x_{\mathrm{Li}})}{\delta x_{\mathrm{Li}}}$ [32,33]. The chemical potential of Li in a fully-ordered spinel $LiMn_2O_4$ remains constant as the spinel is lithiated in the two-phase region, which leads to a voltage plateau of ~1 Li/f.u. near 3 V. However, in partially-disordered $Li_{1.47+x}Mn_{1.6}O_{3.7}F_{0.3}$, the voltage profile is sloping near 3 V, suggesting that the two-phase region is replaced by a solid solution reaction. *Ex-situ* synchrotron XRD in Figure 10 further corroborates that both $Li_{1.47}Mn_{1.6}O_{3.7}F_{0.3}$ and $Li_2Mn_{1.6}O_{3.7}F_{0.3}$ retain cubic symmetry and are free of two phases when discharged to 2.9 and 2.7 V. The suppression of the two-phase region is consistent with fundamental ideas in statistical mechanics which have shown that at critical levels of site-energy disorder, a first order transition first collapses into a second order transition, and then becomes even fully suppressed for even larger site disorder.[34,35] In our materials the Mn 16c/16d disorder creates a statistical distribution of local environments which creates the site-energy disorder for Li and results in a sloping voltage profile.[32,33] Therefore, as x increases from 0.47 to 2, a very broad hump gradually appears in the dQ/dV plots and more capacity is delivered above 3 V (Figure 5).

Consistent with our understanding of percolation in partially disordered spinels versus disordered rocksalts, rate capability is also affected by the cation order. In all but layered cathode

materials,[36] Li transport occurs through so-called 0-TM channels, which are tetrahedral sites that do not face-share with any TMs and their percolation.[3,37] Cation order in a rocksalt-type structure strongly affects the amount of such 0-TM channels and their percolation.[3,37-41] Of all the well-known cation orderings that can be found in a rocksalt host,[42] spinel has the most favorable TM ordering for creating 0-TM channels, making it tolerant to a substantial amount of cation disorder. Figure 11a shows the calculated 0-TM percolated Li capacity in a rocksalt-type structure containing 20% Li-for-Mn substitution, when a fully spinel-ordered cation sublattice becomes increasingly disordered (black dots). The results are compared with those in a layered structure with the same Li-excess (red squares). As shown by these percolation simulations, the structure with a spinel-like cation order always has a higher accessible Li capacity, which monotonously decreases with cation disorder and eventually converges with that of the layered structure at complete cation disorder (that is, a DRX structure), rationalizing its high rate capability.

Finally, spinel-type ordering seems to have a previously unrecognized benefit in that it suppresses oxygen redox. We find that the amount of reversible O redox used in the spinel cathodes with various degrees of cation order is different, even though they have the same Mn content and the same average anion valence. As shown from the O *K*-edge mRIXS results in Figure 9, the more cation-disordered $Li_2Mn_{1.6}O_{3.7}F_{0.3}$ exhibits a stronger oxidized O feature at high voltage than the more spinel-like-ordered $Li_{1.47}Mn_{1.6}O_{3.7}F_{0.3}$. To elucidate the origin of such difference, we computationally analyzed the local environments surrounding O ions in a $Li_xMn_{1.6}O_{3.7}F_{0.3}$ spinel with an increasing degree of cation disorder. We focus on the linear Li-O-Li configurations in the structures because they are a major contributor to the unhybridized high-energy orphaned O states, which can be oxidized and reduced in a typical electrochemical

voltage window.[12] In our simulations, we treat Li and vacancies as equivalent (Li-O-Li = Vacancy-O-Li = Vacancy-O-Vacancy) since neither hybridizes with the O 2*p* orbitals. We find that at 0% disorder, that is, Mn ions confined to the 16d sites, nearly 50% of O ions already have at least one Li-O-Li configuration. More disorder on the cation sublattice transfers Mn ions to the 16c sites until 16c and 16d are equally occupied for the case of 100% cation mixing. In this fully random state the fraction of O ions with at least one Li-O-Li configuration is increased to > 70% (Figure 11b). These results suggest that cation disorder increases the occurrence of Li-rich local environments around O ions makes a higher fraction of them prone to oxidation, consistent with our observation in mRIXS (Figure 9).

Conclusions

In this work, we successfully synthesized a series of Mn-based $Li_{1.4+x}Mn_{1.6}O_{3.7}F_{0.3}$ oxyfluorides with a varying degree of cation order (x = 0.07, 0.28, 0.6, and 1.0) through a mechanochemical method. High specific energy density > 1,000 Wh kg^{-1} (specific capacity > 350 mAh g^{-1}) is achieved in the three partially-(dis)ordered spinel cathodes with significant contribution from reversible O redox. As the Li-over-stoichiometry x in the synthesis increases, the structure transitions from mostly spinel-type to more disordered rocksalt. The cation disorder suppresses the two-phase region associated with the voltage plateau near 3 V and converts it into a solid solution. Through its effect on the local environments the tunable cation order also has a profound effect on rate capability, voltage profile, and redox mechanism. $Li_{1.47}Mn_{1.6}O_{3.7}F_{0.3}$ was found to exhibit the highest rate capability with > 158 mAh g^{-1} delivered at 7.5 A g^{-1}, while the more rocksalt-like $Li_2Mn_{1.6}O_{3.7}F_{0.3}$ utilizes the most O redox in the same voltage window.

Our work emphasizes the importance of exploring the continuum of structure space between well-known ordered compounds. While in our work these materials were produced by mechanochemical synthesis, understanding better how to access thermodynamically stable and metastable partial order by alternative synthesis methods, and how to integrate them into high loading composite cathodes, would be highly desirable to further explore this promising space.

Experimental Procedures

Resource Availability

Lead Contact

Further information and requests for resources and reagents should be directed to and will be fulfilled by the lead contact, Gerbrand Ceder (gceder@berkeley.edu)

Materials Availability

The materials generated in this study are available from the lead contact upon request

Data and Code Availability

All data and code associated with the study have

Materials synthesis and preparation

$LiMn_2O_4$, $Li_{1.47}Mn_{1.6}O_{3.7}F_{0.3}$, $Li_{1.68}Mn_{1.6}O_{3.7}F_{0.3}$, $Li_2Mn_{1.6}O_{3.7}F_{0.3}$ and $Li_{2.4}Mn_{1.6}O_{3.7}F_{0.3}$ were synthesized by high-energy ball-milling. For synthesizing $LiMn_2O_4$ and $Li_{2.4}Mn_{1.6}O_{3.7}F_{0.3}$, one gram of stoichiometric Li_2O, Mn_2O_3, MnO_2, and LiF were mixed into a 50-mL stainless-steel jar with five 10-mm and ten 5-mm stainless-steel balls. The jar was sealed with safety closure clamps in an Ar-filled glove box. After high-energy ball milling at rotational speed of 450 rpm for 10 hours (or 28h), using a Retsch PM200 planetary ball, the phase-pure $LiMn_2O_4$ (or $Li_{2.4}Mn_{1.6}O_{3.7}F_{0.3}$) was obtained. For $Li_{1.47}Mn_{1.6}O_{3.7}F_{0.3}$, $Li_{1.68}Mn_{1.6}O_{3.7}F_{0.3}$ and $Li_2Mn_{1.6}O_{3.7}F_{0.3}$, the precursor Li_2MnO_3 was first synthesized by a solid-state method (firing stoichiometric Li_2CO_3 and MnO_2 at 800 °C in air for 16 hours). Then, stoichiometric Li_2MnO_3, Mn_2O_3, MnO_2 and MnF_2 or MnF_3 were used as precursors. The rest procedure is the same as the previous one except for synthesis time, 21, 24 and 26 hours for $Li_{1.47}Mn_{1.6}O_{3.7}F_{0.3}$, $Li_{1.68}Mn_{1.6}O_{3.7}F_{0.3}$ and $Li_2Mn_{1.6}O_{3.7}F_{0.3}$.

Electrochemistry

All cathode films were fabricated in an Ar-filled glove box. 70 mg active material was first mixed with 20 mg Super C65 carbon black (Timcal) in a mortar by hand for 30 minutes. The components were then mixed with 10 mg polytetrafluoroethylene (Dupont) and rolled into a thin film to be used as a cathode. The cathode was cut by a 5/16 inches-diameter punch and the loading density of the cathode film was 3-4 mg cm^{-2}. To assemble the coin cells (CR2032), 0.1 mL of commercialized 1 M $LiPF_6$ in ethylene carbonate (EC) and dimethyl carbonate (DMC) solution (volume ratio 1:1, Sigma-Aldrich, battery grade) was used as electrolyte, glass microfibers (Whatman) were used as separators and FMC Li round metal foil (7/16 inches in diameter) was used as anode. The assembly process was also carried out in the Ar-filled glove box. After sealing the coin cells, they were rested for 6 hours before being tested on an Arbin battery cycler at room temperature. GITT measurements were performed by charging/discharging the cell for 1 hour at a current density of 10 mA g^{-1} followed by relaxing for 6 h to reach a quasi-equilibrium state.

Structure Characterization

Synchrotron XRD patterns were measured at Beamline 11-BM of Advanced Photon Source. All the *ex-situ* samples were electrode powder composed of active materials and Super C65 in a weight ratio of 9:1. The loose powder mixture was cycled at 5 mA g^{-1}, followed by equilibrating at the designated voltage until the residual current was below 0.2 mA g^{-1}. The cycled powder was then washed with dimethyl carbonate and dried in vacuum. Neutron powder diffraction

experiments were performed at the Spallation Neutron Source in Oak Ridge National Laboratory on the Nanoscale Ordered Materials Diffractometer. All the synchrotron and neutron data refinements were carried out using the TOPAS software package. SEM images were collected using a Zeiss Gemini Ultra-55 Analytical Field Emission SEM at the Molecular Foundry in Lawrence Berkeley National Lab (LBNL). The selected area electron diffraction (SEAD) and HRTEM were collected using a FEI Themis Z probe corrected transmission electron microscope with an accelerating voltage of 200 kV.

Operando Mn K-edge X-ray Absorption Spectroscopy

Operando X-ray absorption spectroscopy (XAS) measurements at Mn K-edge were performed in a transition mode at Beamline 20-BM-B of the Advanced Photon Source, Argonne National Laboratory. A Si (111) monochromator was used for selecting the incident beam energy. A Rh-coated mirror was applied to get harmonic rejection. For the *operando* measurement, the modified *in-situ* cell was cycled within the voltage window of 1.5 - 4.8 V at a cycling rate of 30 mA g^{-1}. All electrode films were made in the same way as described in the electrochemistry section. The energy calibration was accomplished by simultaneously measuring the spectra of Mn metal foil. The cell was held at the top of charge or end of discharge for one hour to ensure a full scan. Normalization and calibration of raw data were carried out by Athena software.[43]

Mapping of resonant inelastic x-ray scattering

mRIXS of O *K*-edge and Mn *L*-edge was measured in the iRIXS endstation at Beamline 8.0.1 of Advanced Light Source,[21] Lawrence Berkeley National Laboratory. The beam spot size is about

25*100 mm^2. Mapping data were collected by the ultrahigh efficiency modular spectrometer,[44] with an excitation energy step of 0.2 eV. The resolution of the excitation energy is 0.35 eV, and that of the emission energy is 0.25 eV. All *ex-situ* samples were electrode films, composed of active materials, carbon black and PTFE in a weight ratio of 70:20:10. The electrode films were charged or discharged to a certain state of charge in a coin cell at 50 mA g^{-1} and held at that voltage for 6 hours. The cells were disassembled, and the films were washed with DEC in an Ar-filled glovebox. Final 2D maps were achieved via a multistep data processing including normalization to beam flux and collecting time, integration and combination, etc., which has been elaborated on in previous work.[9]

Mn-L_3 iPFY

Mn-*L* iPFY was achieved through the formula iPFY = a /PFY_O, where a is a normalization coefficient, PFY_O was extracted by integrating the fluorescence intensity within the O-*K* emission energy range (495 to 510 eV) on the Mn-*L* mRIXS (dotted rectangle in Fig. 2B). Quantitative fitting of Mn-L iPFY was performed via linear combination with the standard experimental spectra of $Mn^{2+/3+/4+}$, as demonstrated and detailed before.[45]

Solid-State Nuclear Magnetic Resonance Spectroscopy (ssNMR)

^{19}F and ^{7}Li ssNMR data were collected on the $Li_{1.47}Mn_{1.6}O_{3.7}F_{0.3}$ and $Li_2Mn_{1.6}O_{3.7}F_{0.3}$ pristine powders using a Bruker Avance 300 MHz (7.05 T) super wide-bore NMR spectrometer with Larmor frequencies of 282.40 MHz and 116.64 MHz, respectively, at room temperature. The data were obtained at 30 kHz magic-angle spinning (MAS) using a 2.5 mm double-resonance

HX probe. ^{19}F and ^{7}Li NMR data were referenced against 1M aqueous solutions of sodium fluoride (NaF, $\delta(^{19}F) = -118$ ppm) and lithium chloride (LiCl, $\delta(^{7}Li) = 0$ ppm) and these samples were also used for pulse calibration. Lineshape analysis was carried out within the Bruker Topspin software using the SOLA lineshape simulation package.

The resonant frequency range of ^{19}F nuclei in $Li_{1.47}Mn_{1.6}O_{3.7}F_{0.3}$ and $Li_2Mn_{1.6}O_{3.7}F_{0.3}$ was larger than the excitation bandwidth of the RF pulse used in the NMR experiment. To obtain the full spectrum, ten spin echo sub-spectra were collected for each sample. These were obtained by varying the carrier frequency in steps of 300 ppm (84.73 kHz) from −1500 to 1200 ppm, where the step size was slightly less than the excitation bandwidth of the RF pulse. Individual sub-spectra were processed using a zero-order phase correction and then added to give an overall sum spectrum in absorption mode that required no further phase correction. This method – termed 'spin echo mapping'[46], 'frequency stepping',[47,48] or 'VOCS' (Variable Offset Cumulative Spectrum)[49] – is able to uniformly excite the broad ^{19}F signals by providing a large excitation bandwidth. Individual ^{19}F spin echo spectra were collected using a 90° RF pulse of 1.95 μs and a 180° RF pulse of 3.9 μs at 190 W, with a recycle delay of 60 ms. Additionally, a ^{19}F spin echo spectrum of LiF was obtained using similar RF pulses for comparison with spectra collected on the partially-(dis)ordered spinel samples using a recycle delay of 5 s at 30 kHz MAS.

^{7}Li spin echo spectra were acquired on all samples using a 90° radiofrequency (RF) pulse of 0.43 μs and a 180° RF pulse of 0.86 μs at 300 W. A recycle delay of 80 ms was used for the partially-(dis)ordered spinel samples. ^{7}Li pj-MATPASS (projected Magic-Angle Turning Phase-Adjusted Sideband Separation)[50] isotropic spectra were also acquired on all samples using a 90° RF pulse of 0.43 μs at 100 W, with a recycle delay of 50 ms.

Differential Electrochemical Mass Spectrometry (DEMS)

Outgassing of $Li_{1.47}Mn_{1.6}O_{3.7}F_{0.3}$ and $Li_2Mn_{1.6}O_{3.7}F_{0.3}$ cathodes during the first cycle of galvanostatic charge of discharge was monitored on a custom-built DEMS system, which was operated as described in a previous study.[51] Modified Swagelok-type cells were prepared in an Ar-filled glove box. The composition of cathodes and anodes were identical to those used for the coin cell tests in this study. For each DEMS cell, one sheet of Celgard 2500 (polypropylene) and one sheet of QM-A quartz microfiber filters (Whatman) were used as separators with 80 µL of 1 M $LiPF_6$ (Gotion) in EC/DEC (BASF, 1:1 v/v) added as the electrolyte. DEMS cells were cycled at a constant current rate of 0.1 Li^+ h^{-1} (16.44 mA g^{-1} for $Li_{1.47}Mn_{1.6}O_{3.7}F_{0.3}$ and 16.08 mA g^{-1} for $Li_2Mn_{1.6}O_{3.7}F_{0.3}$) under a static head of argon pressure (approximately 1.2 bar) at room temperature. Accumulated gas in the cell was purged by 500 µL of pulsed Ar gas every 10 minutes. Swept-out gas was sent to a holding chamber, where it was subsequently leaked to a mass-spectrometry chamber for analysis. The setup is calibrated for O_2 and CO_2 in the carrier gas Ar.

Acknowledgement

This work is supported by the Assistant Secretary for Energy Efficiency and Renewable Energy, Vehicle Technologies Office, under the Applied Battery Materials Program, of the US DOE under contract no. DE-AC02-05CH11231 and by Umicore Specialty Oxides and Chemicals. Work at the Advanced Light Source is supported by the Director, Office of Science, Office of Basic Energy Sciences, of the US DOE under contract no. DE-AC02-05CH11231. Research conducted at the Nanoscale Ordered Materials Diffractometer Beamline at Oak Ridge National Laboratory's Spallation Neutron Source is sponsored by the Scientific User Facilities Division, Office of Basic Sciences of the US DOE. Work at the Molecular Foundry at Lawrence Berkeley National Laboratory is supported by the Office of Science, Office of Basic Energy Sciences of the US DOE under contract no. DE-AC02-05CH11231. This research used resources of the Advanced Photon Source, an Office of Science User Facility operated for the US DOE Office of Science by Argonne National Laboratory, and is supported by the US DOE under contract no. DE-AC02-06CH11357. The NMR experimental work reported here made use of the shared facilities of the UCSB MRSEC (NSF DMR 1720256), a member of the Material Research Facilities Network. E. E. Foley was supported by the NSF Graduate Research Fellowship Program under Grant No. DGE 1650114. T.-Y. Huang was supported collectively by both Ministry of Education in Taiwan and UC Berkeley College of Chemistry through Taiwan Fellowship Program. The authors thank Bin Ouyang and Han-Ming Hau for helpful discussions.

Author contribution

Z.C. planned the project with G.C. and H.J; Z.C. and H.J. designed, synthesized, characterized and electrochemically tested the proposed compounds with help from Z.L., Y.C and J.W.; Y.H. acquired and analyzed the mRIXS data with input from W.Y.; J.L. acquired and analyzed the sXRD and neutron diffraction data; D.-H.K. and Y.Z. acquired and analyzed the TEM data; A.U. performed Monte Calo and DFT calculations and analyzed the data; E.E.F and R.G. acquired and analyzed the NMR data with input from R.J.C.; Z.C. and H.K. acquired and analyzed the XAS data with help from M.B. and Z.L.; T.-Y.H. acquired and analyzed the DEMS data with input from B.D.M; G.Z. performed SEM. The manuscriptal was written by Z.C. and H.J. and was revised by R.J.C., and G.C. with help from the other authors. All authors contributed to discussions.

Declaration of Interests

The authors declare no competing interests.

Figure titles and legends

Figure 1. Design of partially-(dis)ordered spinel cathodes with Li over-stoichiometry *x* and Mn substitution by Li *y*. (a) Structure of fully-ordered $LiMn_2O_4$ (grey octahedra = MnO_6, green tetrahedra = LiO_4, green spheres = Li ions). The atomic slab outlined by the orange square is viewed from above and depicted in detail in (b) as fully ordered (left), with some Mn substituted by Li (middle), and with partial disorder and Li over-stoichiometry. The bold green squares represent face sharing Li_{tet}-Li_{oct}.

Figure 2. Refinement of three partially-(dis)ordered spinels. Rietveld refinement of the crystal structure using (a) synchrotron X-ray diffraction data (λ = 0.4579 Å) and (b) time-of-flight neutron diffraction data, of $Li_{1.47}Mn_{1.6}O_{3.7}F_{0.3}$, $Li_{1.68}Mn_{1.6}O_{3.7}F_{0.3}$ and $Li_2Mn_{1.6}O_{3.7}F_{0.3}$.

Figure 3. SEM, STEM/EDS and HRTEM/ED of two partially-(dis)ordered spinel compounds. SEM images of the as-synthesized (a) $Li_{1.47}Mn_{1.6}O_{3.7}F_{0.3}$ and (b) $Li_2Mn_{1.6}O_{3.7}F_{0.3}$ (scale bars, 200 nm). STEM images and EDS mapping of the elements Mn, O and F (c) $Li_{1.47}Mn_{1.6}O_{3.7}F_{0.3}$ and (d) $Li_2Mn_{1.6}O_{3.7}F_{0.3}$ (scale bars, 30 nm). HRTEM images of (e) $Li_{1.47}Mn_{1.6}O_{3.7}F_{0.3}$ and (f) $Li_2Mn_{1.6}O_{3.7}F_{0.3}$ (scale bars, 10 nm). Insets: ED patterns (scale bars, 5 nm^{-1}). The selected area electron diffraction patterns can be indexed to a spinel lattice, with the *d* spacings measured to be 4.8, 2.5, 2.1, 1.6, 1.5, 1.2 and 1.0 Å.

Figure 4. ssNMR spectra obtained on the as-synthesized partially-(dis)ordered spinel materials. (a) ^{19}F ssNMR spectra obtained by summing multiple spin echo sub-spectra acquired at different excitation frequencies to ensure homogeneous excitation of the broad lineshape. For comparison, a ^{19}F spectrum collected on LiF powder is overlaid. (b) ^{7}Li spin echo (line) and pj-MATPASS (shaded, for clarity) ssNMR spectra of the as-synthesized materials. All spectra are scaled according to the moles of Li in the rotor and number of scans. The asterisks indicate the spinning sidebands.

Figure 5. Galvanostatic charge and discharge performance. (a) voltage profile during first cycle and the second charge of $Li_{1.47}Mn_{1.6}O_{3.7}F_{0.3}$ (black dash dot), $Li_{1.68}Mn_{1.6}O_{3.7}F_{0.3}$ (blue dot) and $Li_2Mn_{1.6}O_{3.7}F_{0.3}$ (red dash). (b) Corresponding dQ/dV curves when cycled between 1.5 and 4.8 V at 50 mA g^{-1}.

Figure 6. Galvanostatic cycling performance. Voltage profiles during the first 5 cycles of (a) $Li_{1.47}Mn_{1.6}O_{3.7}F_{0.3}$, (b) $Li_{1.68}Mn_{1.6}O_{3.7}F_{0.3}$, and (c) $Li_2Mn_{1.6}O_{3.7}F_{0.3}$. The initial discharge capacity, energy density and average discharge voltage are denoted in each figure. Capacity retention and Coulombic efficiency over 30 cycles of (d) $Li_{1.47}Mn_{1.6}O_{3.7}F_{0.3}$, (e) $Li_{1.68}Mn_{1.6}O_{3.7}F_{0.3}$, and (f) $Li_2Mn_{1.6}O_{3.7}F_{0.3}$, in two voltage ranges, 1.5 – 4.8V (red open squares) and 2 – 4.4 V (blue open circles).

Figure 7. Rate capability measurements. (a) Galvanostatic voltage profiles of (top to bottom) $LiMn_2O_4$, $Li_{1.47}Mn_{1.6}O_{3.7}F_{0.3}$, $Li_{1.68}Mn_{1.6}O_{3.7}F_{0.3}$, $Li_2Mn_{1.6}O_{3.7}F_{0.3}$, and $Li_{2.4}Mn_{1.6}O_{3.7}F_{0.3}$ at

various rates, from 100 to 7,500 mA g^{-1}. (b) Ragone plot comparing the specific energy and power. The loading density of the cathode films was 2-3 mg cm^{-2}, containing 70 wt% active materials, 20 wt% carbon black and 10 wt% Teflon.

Figure 8. Redox mechanism of $Li_{1.47}Mn_{1.6}O_{3.7}F_{0.3}$ and $Li_2Mn_{1.6}O_{3.7}F_{0.3}$. Operando Mn K-edge X-ray absorption near edge spectra (XANES) of (a) $Li_{1.47}Mn_{1.6}O_{3.7}F_{0.3}$ and (b) $Li_2Mn_{1.6}O_{3.7}F_{0.3}$ during the first cycle and second charge. The blue, red, olive and orange curves represent the pristine, first charge to 4.8 V (1C4.8V), first discharge to 1.5 V (1DC1.5V) and second charge to 4.8 V (2C4.8V), respectively. *Ex-situ* Mn L_3-edge mRIXS-iPFY spectra of (c) $Li_{1.47}Mn_{1.6}O_{3.7}F_{0.3}$ and (d) $Li_2Mn_{1.6}O_{3.7}F_{0.3}$ at seven states of charge and discharge during the first and second cycle. Standard spectra of Mn^{2+}, Mn^{3+} and Mn^{4+} are included as references. The dash vertical lines highlight peak positions based on the standard spectra. Quantification of Mn valance (blue squares) based on mRIXS-iPFY overlaid on voltage profiles (black curves) during the first cycle in (e) $Li_{1.47}Mn_{1.6}O_{3.7}F_{0.3}$ and (f) $Li_2Mn_{1.6}O_{3.7}F_{0.3}$.

Figure 9. O Redox mechanism investigated by mapping of resonant inelastic X-ray scattering (mRIXS)**.** a. *Ex-situ* O K-edge mRIXS at selected states during the first cycle and the top of charge during the second cycle (top to bottom). Along the vertical axis is the excitation energy with a 1 eV window around 531 eV. b. Corresponding O mRIXS cuts at 531.0 eV excitation energy.

Figure 10. *Ex-situ* synchrotron XRD of cycled cathode samples. Synchrotron XRD patterns of the pristine and cycled samples of (a) $Li_{1.47}Mn_{1.6}O_{3.7}F_{0.3}$ and (b) $Li_2Mn_{1.6}O_{3.7}F_{0.3}$ The selected states of charge are pristine, first-cycle discharge to 2.9 V (red) and 2.7 V (blue). The green bar indicates the diffraction peak of spinel structure.

Figure 11. Amount of accessible Li and O local environments as a function of cation mixing (or disorder). a. The amount of kinetically accessible Li through 0-TM percolation in $Li_{2.4}TM_{1.6}O_{3.7}F_{0.3}$ varies with the degree of cation mixing for spinel-type (black dots) or layered (red squares) cation arrangement. The two plots converge at 100% cation mixing, which corresponds to complete cation disorder. b. The fraction of O atoms that have at least 1 linear Li-O-Li, at least 2 linear Li-O-Li or 3 linear Li-O-Li configurations in $Li_{2.4}TM_{1.6}O_4$. The influence of the low-level fluorination is neglected.

Table

Table 1. Structural information based on synchrotron and neutron powder diffraction refinement.

Atom	Wyckoff symbol	*x*	*y*	*z*	B_{iso}	$Li_{1.47}Mn_{1.6}O_{3.7}F_{0.3}$ occupancy	$Li_{1.68}Mn_{1.6}O_{3.7}F_{0.3}$ occupancy	$Li_2Mn_{1.6}O_{3.7}F_{0.3}$ occupancy
Li1	8a	0.125	0.125	0.125	0.80(2)	0.65(5)	0.57(5)	0.18(6)
Li2	16d	0.5	0.5	0.5	0.80(2)	0.10(2)	0.25(2)	0.44(2)
Li3	16c	0	0	0	0.80(2)	0.31(2)	0.31(2)	0.47(2)
Mn1	16d	0.5	0.5	0.5	0.83(9)	0.74(2)	0.67(5)	0.56(2)
Mn2	16c	0	0	0	0.83(9)	0.06(2)	0.12(5)	0.24(2)
O1	32e	0.259(3)	0.259(3)	0.259(3)	0.66(3)	0.925	0.925	0.925
F1	32e	0.259(3)	0.259(3)	0.259(3)	0.66(3)	0.075	0.075	0.075

References

1. Olivetti, E.A., Ceder, G., Gaustad, G.G., and Fu, X. (2017). Lithium-ion battery supply chain considerations: analysis of potential bottlenecks in critical metals. Joule *1*, 229-243.
2. Reed, J., Ceder, G., and Van Der Ven, A. (2001). Layered-to-spinel phase transition in Li x MnO2. Electrochemical and Solid State Letters *4*, A78.
3. Urban, A., Lee, J., and Ceder, G. (2014). The Configurational Space of Rocksalt‐Type Oxides for High‐Capacity Lithium Battery Electrodes. Advanced Energy Materials *4*, 1400478.
4. Lee, E., and Persson, K.A. (2013). Solid-Solution Li Intercalation as a Function of Cation Order/Disorder in the High-Voltage Li x Ni0. 5Mn1. 5O4 Spinel. Chemistry of Materials *25*, 2885-2889.
5. Lee, E.-S., Nam, K.-W., Hu, E., and Manthiram, A. (2012). Influence of cation ordering and lattice distortion on the charge–discharge behavior of LiMn1. 5Ni0. 5O4 spinel between 5.0 and 2.0 V. Chemistry of Materials *24*, 3610-3620.
6. Bianchini, M., Suard, E., Croguennec, L., and Masquelier, C. (2014). Li-Rich Li1+ x Mn2–x O4 Spinel Electrode Materials: An Operando Neutron Diffraction Study during Li+ Extraction/Insertion. The Journal of Physical Chemistry C *118*, 25947-25955.
7. Liu, Y., Liu, G., Xu, H., Zheng, Y., Huang, Y., Li, S., and Li, J. (2019). Low-Temperature Synthesized Li4Mn5O12-Like Cathode with Hybrid Cation-and Anion-Redox Capacities. Chemical Communications.
8. Thackeray, M.M., De Kock, A., Rossouw, M.H., Liles, D., Bittihn, R., and Hoge, D. (1992). Spinel electrodes from the Li‐Mn‐O system for rechargeable lithium battery applications. Journal of The Electrochemical Society *139*, 363.
9. Ji, H., Wu, J., Cai, Z., Liu, J., Kwon, D.-H., Kim, H., Urban, A., Papp, J.K., Foley, E., Tian, Y., et al. (2020). Ultrahigh power and energy density in partially ordered lithium-ion cathode materials. Nature Energy. 10.1038/s41560-020-0573-1.
10. Lun, Z., Ouyang, B., Kitchaev, D.A., Clément, R.J., Papp, J.K., Balasubramanian, M., Tian, Y., Lei, T., Shi, T., and McCloskey, B.D. (2019). Improved Cycling Performance of Li‐Excess Cation‐Disordered Cathode Materials upon Fluorine Substitution. Advanced Energy Materials *9*, 1802959.
11. Lee, J., Papp, J.K., Clément, R.J., Sallis, S., Kwon, D.-H., Shi, T., Yang, W., McCloskey, B.D., and Ceder, G. (2017). Mitigating oxygen loss to improve the cycling performance of high capacity cation-disordered cathode materials. Nature communications *8*, 981.
12. Seo, D.-H., Lee, J., Urban, A., Malik, R., Kang, S., and Ceder, G. (2016). The structural and chemical origin of the oxygen redox activity in layered and cation-disordered Li-excess cathode materials. Nature chemistry *8*, 692.
13. Lee, J., Kitchaev, D.A., Kwon, D.-H., Lee, C.-W., Papp, J.K., Liu, Y.-S., Lun, Z., Clément, R.J., Shi, T., and McCloskey, B.D. (2018). Reversible Mn 2+/Mn 4+ double redox in lithium-excess cathode materials. Nature *556*, 185.
14. Kitchaev, D.A., Lun, Z., Richards, W.D., Ji, H., Clément, R.J., Balasubramanian, M., Kwon, D.-H., Dai, K., Papp, J.K., and Lei, T. (2018). Design principles for high transition metal capacity in disordered rocksalt Li-ion cathodes. Energy & Environmental Science *11*, 2159-2171.
15. Zhang, W., Seo, D.-H., Chen, T., Wu, L., Topsakal, M., Zhu, Y., Lu, D., Ceder, G., and Wang, F. (2020). Kinetic pathways of ionic transport in fast-charging lithium titanate. Science *367*, 1030-1034.
16. Yue, Y., Li, N., Ha, Y., Crafton, M.J., McCloskey, B.D., Yang, W., and Tong, W. (2021). Tailoring the Redox Reactions for High‐Capacity Cycling of Cation‐Disordered Rocksalt Cathodes. Advanced Functional Materials, 2008696.
17. Richards, W.D., Dacek, S.T., Kitchaev, D.A., and Ceder, G. (2018). Fluorination of Lithium‐Excess Transition Metal Oxide Cathode Materials. Advanced Energy Materials *8*, 1701533.

18. Thackeray, M.M., David, W.I.F., Bruce, P.G., and Goodenough, J.B. (1983). Lithium insertion into manganese spinels. Materials Research Bulletin *18*, 461-472.
19. (!!! INVALID CITATION !!! 19,20).
20. Yang, W., and Devereaux, T.P. (2018). Anionic and cationic redox and interfaces in batteries: Advances from soft X-ray absorption spectroscopy to resonant inelastic scattering. Journal of Power Sources *389*, 188-197.
21. Qiao, R., Li, Q., Zhuo, Z., Sallis, S., Fuchs, O., Blum, M., Weinhardt, L., Heske, C., Pepper, J., and Jones, M. (2017). High-efficiency in situ resonant inelastic x-ray scattering (iRIXS) endstation at the Advanced Light Source. Review of Scientific Instruments *88*, 033106.
22. Achkar, A.J., Regier, T.Z., Wadati, H., Kim, Y.J., Zhang, H., and Hawthorn, D.G. (2011). Bulk sensitive x-ray absorption spectroscopy free of self-absorption effects. Physical Review B *83*, 081106.
23. Luo, K., Roberts, M.R., Guerrini, N., Tapia-Ruiz, N., Hao, R., Massel, F., Pickup, D.M., Ramos, S., Liu, Y.-S., and Guo, J. (2016). Anion redox chemistry in the cobalt free 3d transition metal oxide intercalation electrode Li [Li0. 2Ni0. 2Mn0. 6] O2. Journal of the American Chemical Society *138*, 11211-11218.
24. Sathiya, M., Rousse, G., Ramesha, K., Laisa, C.P., Vezin, H., Sougrati, M.T., Doublet, M.-L., Foix, D., Gonbeau, D., and Walker, W. (2013). Reversible anionic redox chemistry in high-capacity layered-oxide electrodes. Nature materials *12*, 827.
25. Dai, K., Wu, J., Zhuo, Z., Li, Q., Sallis, S., Mao, J., Ai, G., Sun, C., Li, Z., and Gent, W.E. (2019). High Reversibility of Lattice Oxygen Redox Quantified by Direct Bulk Probes of Both Anionic and Cationic Redox Reactions. Joule *3*, 518-541.
26. Zhuo, Z., Pemmaraju, C.D., Vinson, J., Jia, C., Moritz, B., Lee, I., Sallies, S., Li, Q., Wu, J., and Dai, K. (2018). Spectroscopic signature of oxidized oxygen states in peroxides. The journal of physical chemistry letters *9*, 6378-6384.
27. Tian, Y., Zeng, G., Rutt, A., Shi, T., Kim, H., Wang, J., Koettgen, J., Sun, Y., Ouyang, B., and Chen, T. (2020). Promises and Challenges of Next-Generation "Beyond Li-ion" Batteries for Electric Vehicles and Grid Decarbonization. Chemical reviews.
28. Manthiram, A. (2020). A reflection on lithium-ion battery cathode chemistry. Nature Communications *11*, 1-9.
29. Lun, Z., Ouyang, B., Kwon, D.-H., Ha, Y., Foley, E.E., Huang, T.-Y., Cai, Z., Kim, H., Balasubramanian, M., and Sun, Y. (2020). Cation-disordered rocksalt-type high-entropy cathodes for Li-ion batteries. Nature Materials, 1-8.
30. Clément, R.J., Lun, Z., and Ceder, G. (2020). Cation-disordered rocksalt transition metal oxides and oxyfluorides for high energy lithium-ion cathodes. Energy & Environmental Science.
31. Lee, J., Urban, A., Li, X., Su, D., Hautier, G., and Ceder, G. (2014). Unlocking the potential of cation-disordered oxides for rechargeable lithium batteries. Science *343*, 519-522.
32. Abdellahi, A., Urban, A., Dacek, S., and Ceder, G. (2016). Understanding the effect of cation disorder on the voltage profile of lithium transition-metal oxides. Chemistry of Materials *28*, 5373-5383.
33. Abdellahi, A., Urban, A., Dacek, S., and Ceder, G. (2016). The effect of cation disorder on the average Li intercalation voltage of transition-metal oxides. Chemistry of Materials *28*, 3659-3665.
34. Fisher, M.E., and Berker, A.N. (1982). Scaling for first-order phase transitions in thermodynamic and finite systems. Physical Review B *26*, 2507.
35. Nienhuis, B., Berker, A.N., Riedel, E.K., and Schick, M. (1979). First-and second-order phase transitions in Potts models: renormalization-group solution. Physical Review Letters *43*, 737.
36. Van der Ven, A., Deng, Z., Banerjee, S., and Ong, S.P. (2020). Rechargeable Alkali-Ion Battery Materials: Theory and Computation. Chemical Reviews.
37. Ji, H., Urban, A., Kitchaev, D.A., Kwon, D.-H., Artrith, N., Ophus, C., Huang, W., Cai, Z., Shi, T., and Kim, J.C. (2019). Hidden structural and chemical order controls lithium transport in cation-disordered oxides for rechargeable batteries. Nature communications *10*, 592.

38. Zhong, P., Cai, Z., Zhang, Y., Giovine, R., Ouyang, B., Zeng, G., Chen, Y., Clément, R.l., Lun, Z., and Ceder, G. (2020). Increasing Capacity in Disordered Rocksalt Cathodes by Mg Doping. Chemistry of Materials.
39. Ouyang, B., Artrith, N., Lun, Z., Jadidi, Z., Kitchaev, D.A., Ji, H., Urban, A., and Ceder, G. (2020). Effect of Fluorination on Lithium Transport and Short‐Range Order in Disordered‐Rocksalt‐Type Lithium‐Ion Battery Cathodes. Advanced Energy Materials, 1903240.
40. Lun, Z., Ouyang, B., Cai, Z., Clément, R.J., Kwon, D.-H., Huang, J., Papp, J.K., Balasubramanian, M., Tian, Y., and McCloskey, B.D. (2019). Design Principles for High-Capacity Mn-Based Cation-Disordered Rocksalt Cathodes. Chem.
41. Clément, R.J., Kitchaev, D., Lee, J., and Ceder, G. (2018). Short-range order and unusual modes of nickel redox in a fluorine-substituted disordered rocksalt oxide lithium-ion cathode. Chemistry of Materials *30*, 6945-6956.
42. Wu, E.J., Tepesch, P.D., and Ceder, G. (1998). Size and charge effects on the structural stability of LiMO2 (M= transition metal) compounds. Philosophical Magazine B *77*, 1039-1047.
43. Ravel, B., and Newville, M. (2005). ATHENA, ARTEMIS, HEPHAESTUS: data analysis for X-ray absorption spectroscopy using IFEFFIT. Journal of synchrotron radiation *12*, 537-541.
44. Chuang, Y.-D., Shao, Y.-C., Cruz, A., Hanzel, K., Brown, A., Frano, A., Qiao, R., Smith, B., Domning, E., and Huang, S.-W. (2017). Modular soft x-ray spectrometer for applications in energy sciences and quantum materials. Review of Scientific Instruments *88*, 013110.
45. Li, Q., Qiao, R., Wray, L.A., Chen, J., Zhuo, Z., Chen, Y., Yan, S., Pan, F., Hussain, Z., and Yang, W. (2016). Quantitative probe of the transition metal redox in battery electrodes through soft x-ray absorption spectroscopy. Journal of Physics D: Applied Physics *49*, 413003.
46. Sananes, M.T., Tuel, A., Volta, J.C., and Hutchings, G.J. (1994). Characterization of different precursors and activated vanadium phosphate catalysts by [sup 31] P NMR spin echo mapping. Journal of Catalysis;(United States) *148*.
47. O'Dell, L.A., Rossini, A.J., and Schurko, R.W. (2009). Acquisition of ultra-wideline NMR spectra from quadrupolar nuclei by frequency stepped WURST–QCPMG. Chemical physics letters *468*, 330-335.
48. Pell, A.J., Clément, R.J., Grey, C.P., Emsley, L., and Pintacuda, G. (2013). Frequency-stepped acquisition in nuclear magnetic resonance spectroscopy under magic angle spinning. The Journal of chemical physics *138*, 114201.
49. Massiot, D., Farnan, I., Gautier, N., Trumeau, D., Trokiner, A., and Coutures, J.P. (1995). 71Ga and 69Ga nuclear magnetic resonance study of β-Ga2O3: resolution of four-and six-fold coordinated Ga sites in static conditions. Solid State Nuclear Magnetic Resonance *4*, 241-248.
50. Hung, I., Zhou, L., Pourpoint, F.d.r., Grey, C.P., and Gan, Z. (2012). Isotropic high field NMR spectra of Li-ion battery materials with anisotropy> 1 MHz. Journal of the American Chemical Society *134*, 1898-1901.
51. McCloskey, B.D., Bethune, D.S., Shelby, R.M., Girishkumar, G., and Luntz, A.C. (2011). Solvents' critical role in nonaqueous lithium–oxygen battery electrochemistry. The Journal of Physical Chemistry Letters *2*, 1161-1166.

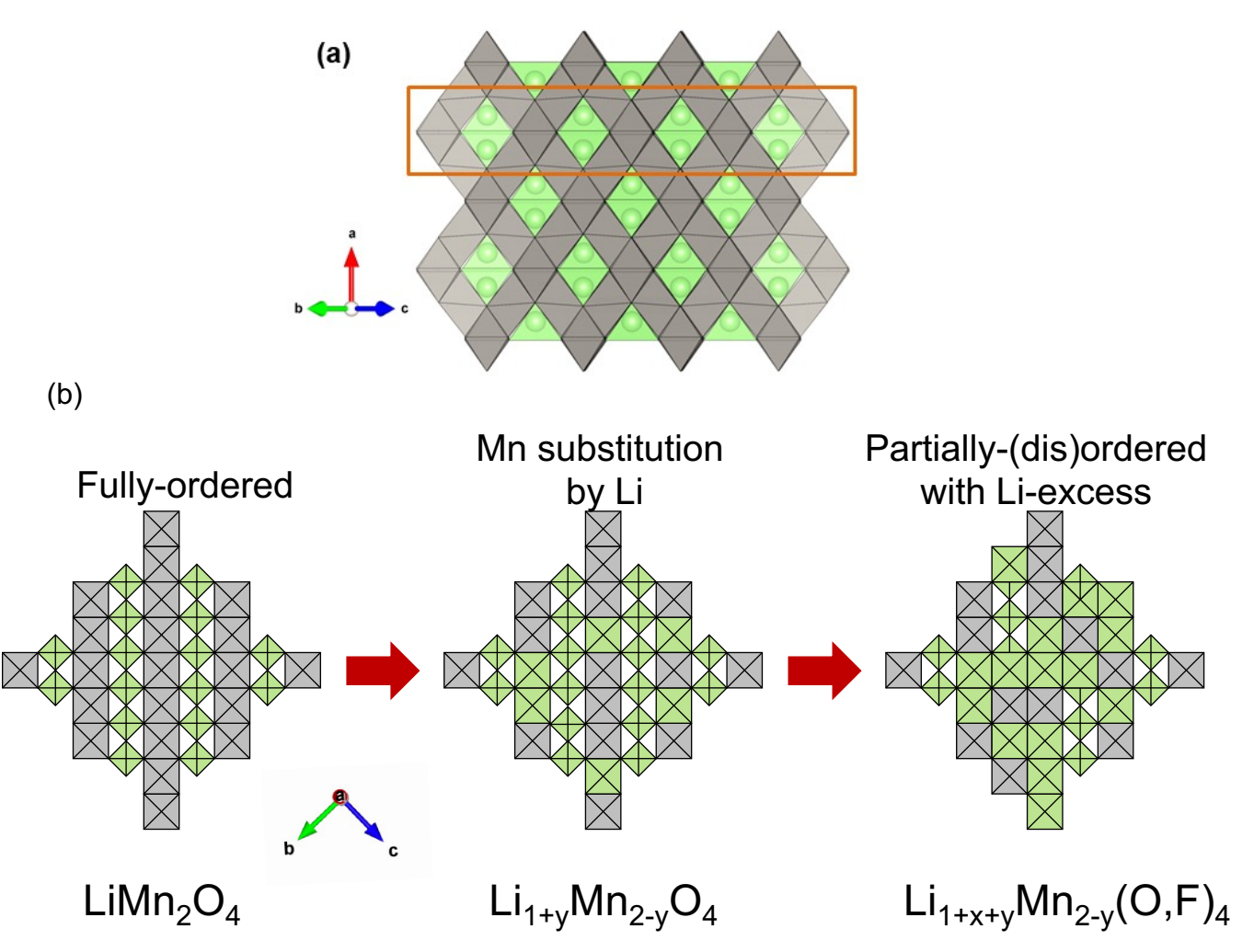
(a)
a
b
c
(b)
Fully-ordered
Mn substitution by Li
Partially-(dis)ordered with Li-excess
a
b
c
$LiMn_2O_4$
$Li_{1+y}Mn_{2-y}O_4$
$Li_{1+x+y}Mn_{2-y}(O,F)_4$

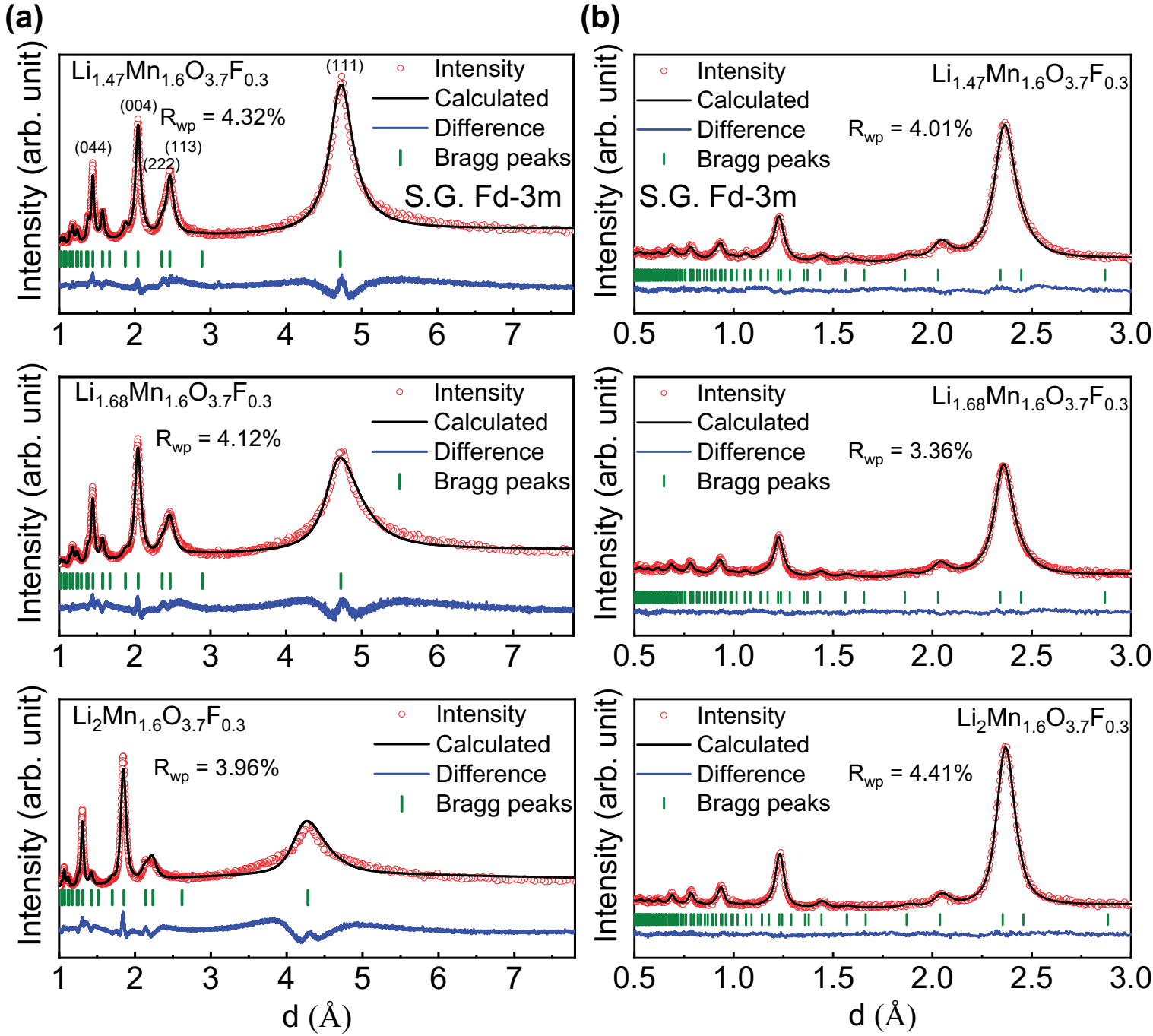
(a)
(b)
Li1.47Mn1.6O3.7F0.3
Rwp = 4.32%
(044)
(004)
(222)
(113)
(111)
S.G. Fd-3m
Intensity
Calculated
Difference
Bragg peaks
Rwp = 4.01%
Li1.68Mn1.6O3.7F0.3
Rwp = 4.12%
Rwp = 3.36%
Li2Mn1.6O3.7F0.3
Rwp = 3.96%
Rwp = 4.41%
Intensity (arb. unit)
d (Å)

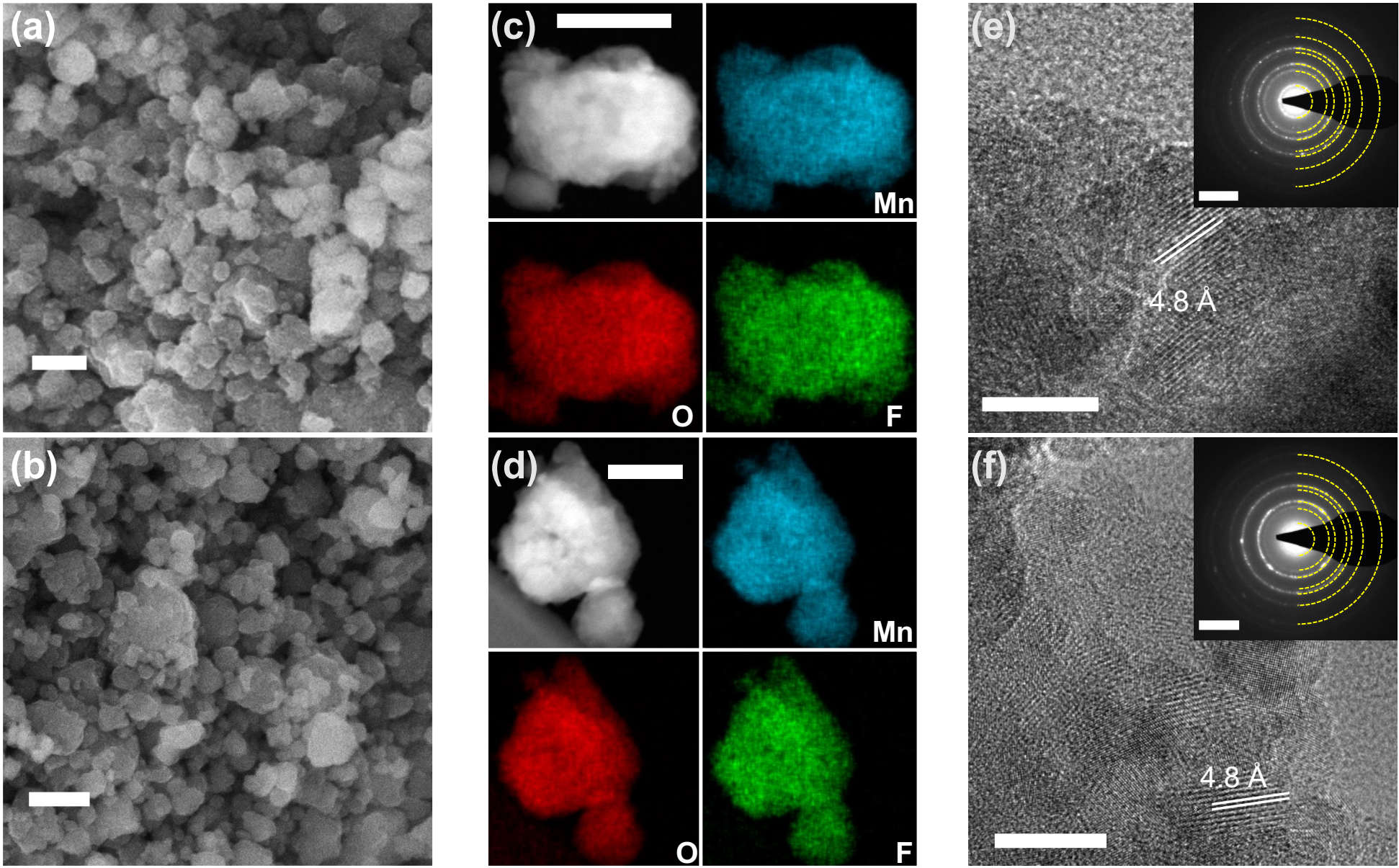
(a)
(b)
(c)
Mn
O
F
(d)
Mn
O
F
(e)
4.8 Å
(f)
4.8 Å

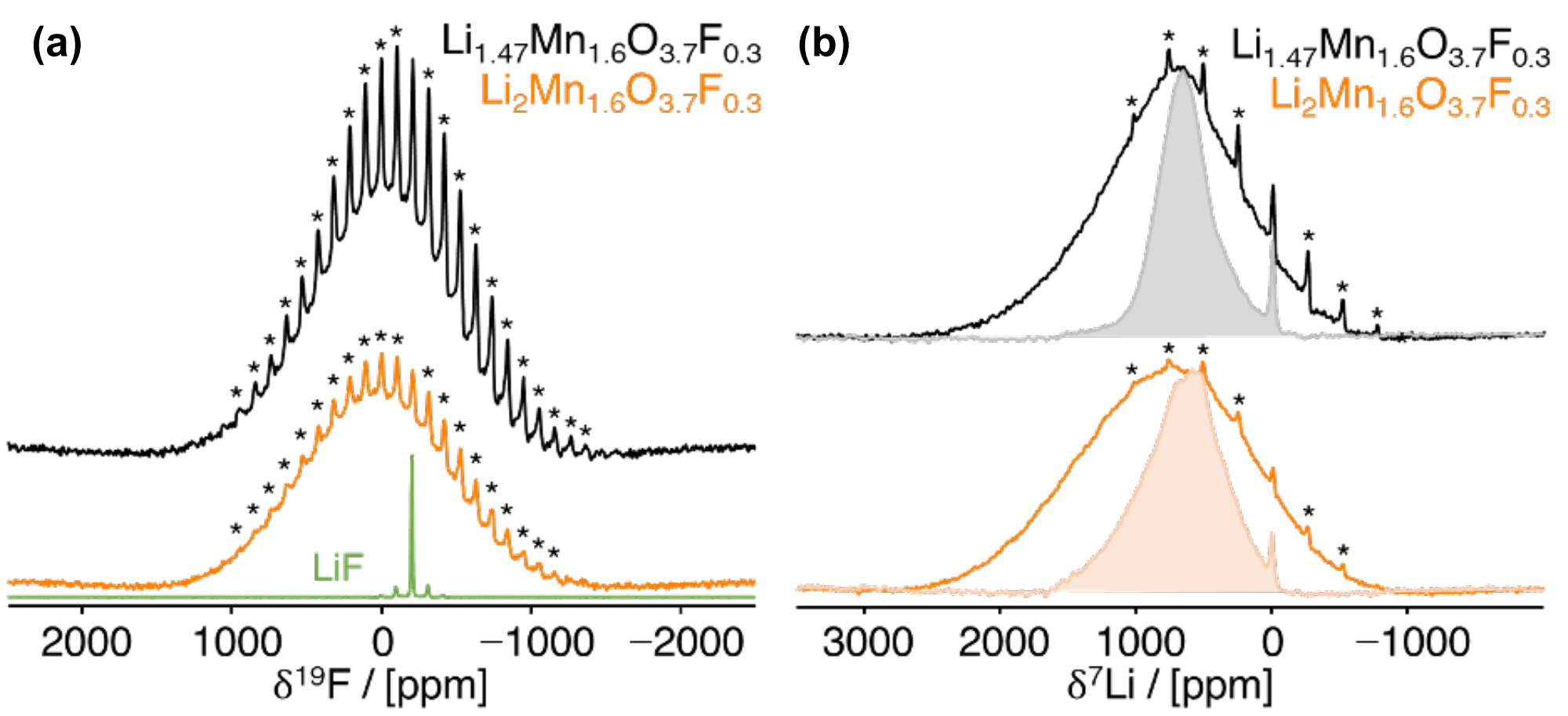
(a)
Li1.47Mn1.6O3.7F0.3
Li2Mn1.6O3.7F0.3
LiF
2000
1000
0
−1000
−2000
δ19F / [ppm]
(b)
Li1.47Mn1.6O3.7F0.3
Li2Mn1.6O3.7F0.3
3000
2000
1000
0
−1000
δ7Li / [ppm]

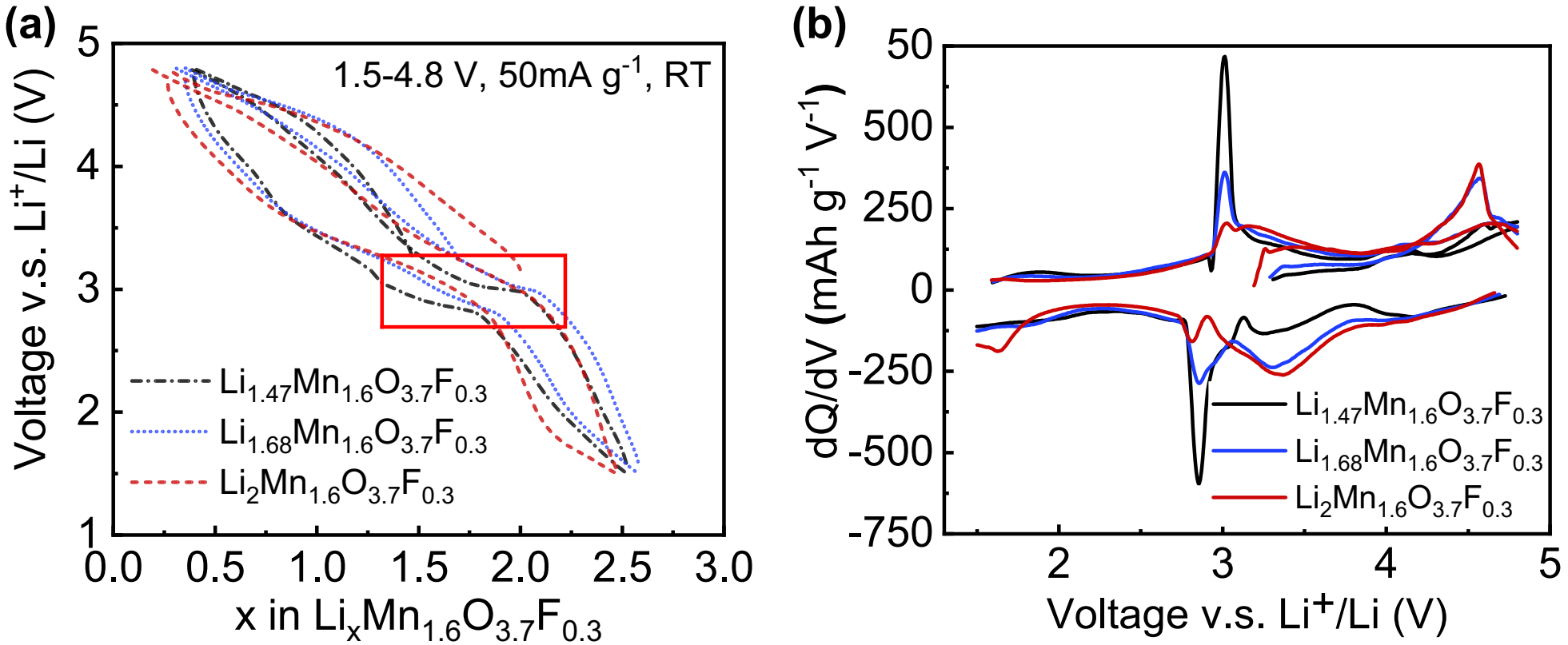
(a)
1.5-4.8 V, 50mA g-1, RT
Voltage v.s. Li+/Li (V)
x in LixMn1.6O3.7F0.3
Li1.47Mn1.6O3.7F0.3
Li1.68Mn1.6O3.7F0.3
Li2Mn1.6O3.7F0.3
(b)
dQ/dV (mAh g-1 V-1)
Voltage v.s. Li+/Li (V)
Li1.47Mn1.6O3.7F0.3
Li1.68Mn1.6O3.7F0.3
Li2Mn1.6O3.7F0.3

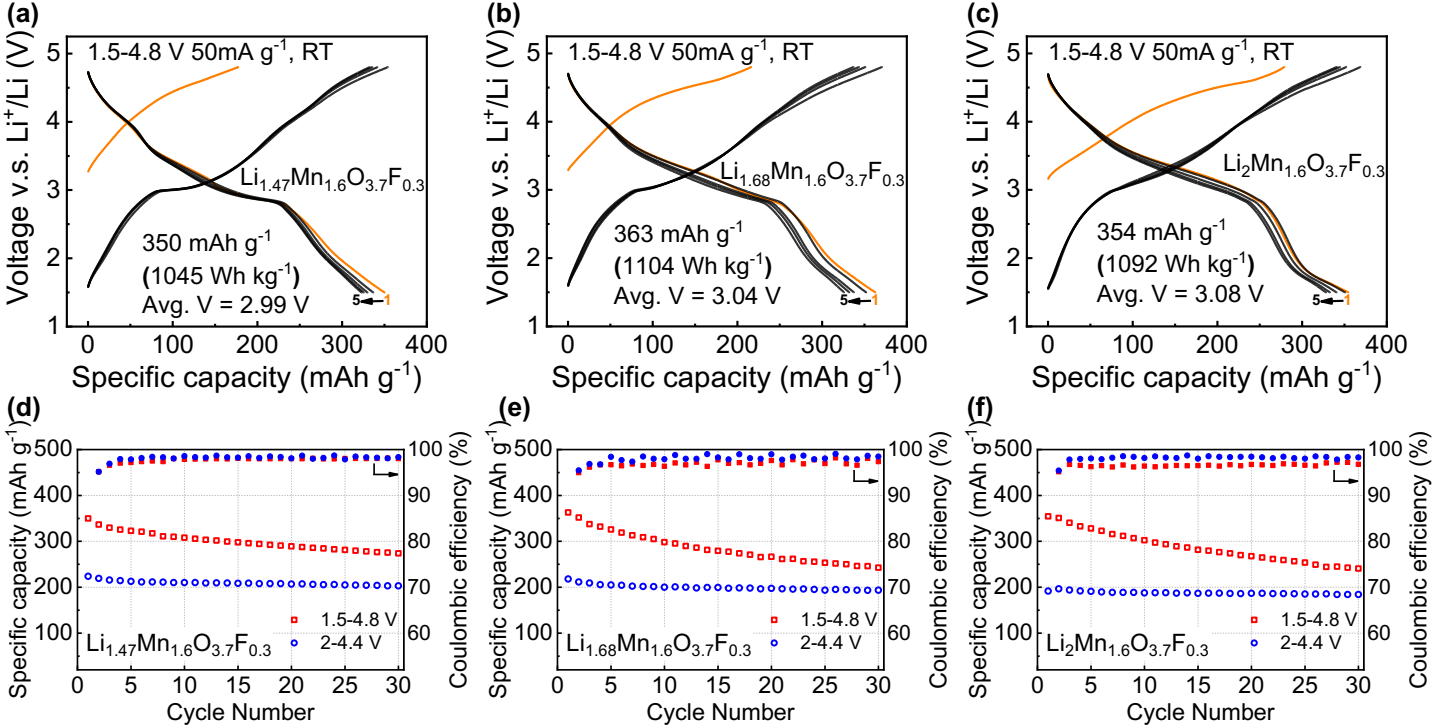
(a)
1.5-4.8 V 50mA g-1, RT
Li1.47Mn1.6O3.7F0.3
350 mAh g-1
(1045 Wh kg-1)
Avg. V = 2.99 V
(b)
1.5-4.8 V 50mA g-1, RT
Li1.68Mn1.6O3.7F0.3
363 mAh g-1
(1104 Wh kg-1)
Avg. V = 3.04 V
(c)
1.5-4.8 V 50mA g-1, RT
Li2Mn1.6O3.7F0.3
354 mAh g-1
(1092 Wh kg-1)
Avg. V = 3.08 V
Voltage v.s. Li+/Li (V)
Specific capacity (mAh g-1)
(d)
(e)
(f)
Specific capacity (mAh g-1)
Coulombic efficiency (%)
1.5-4.8 V
2-4.4 V
Cycle Number

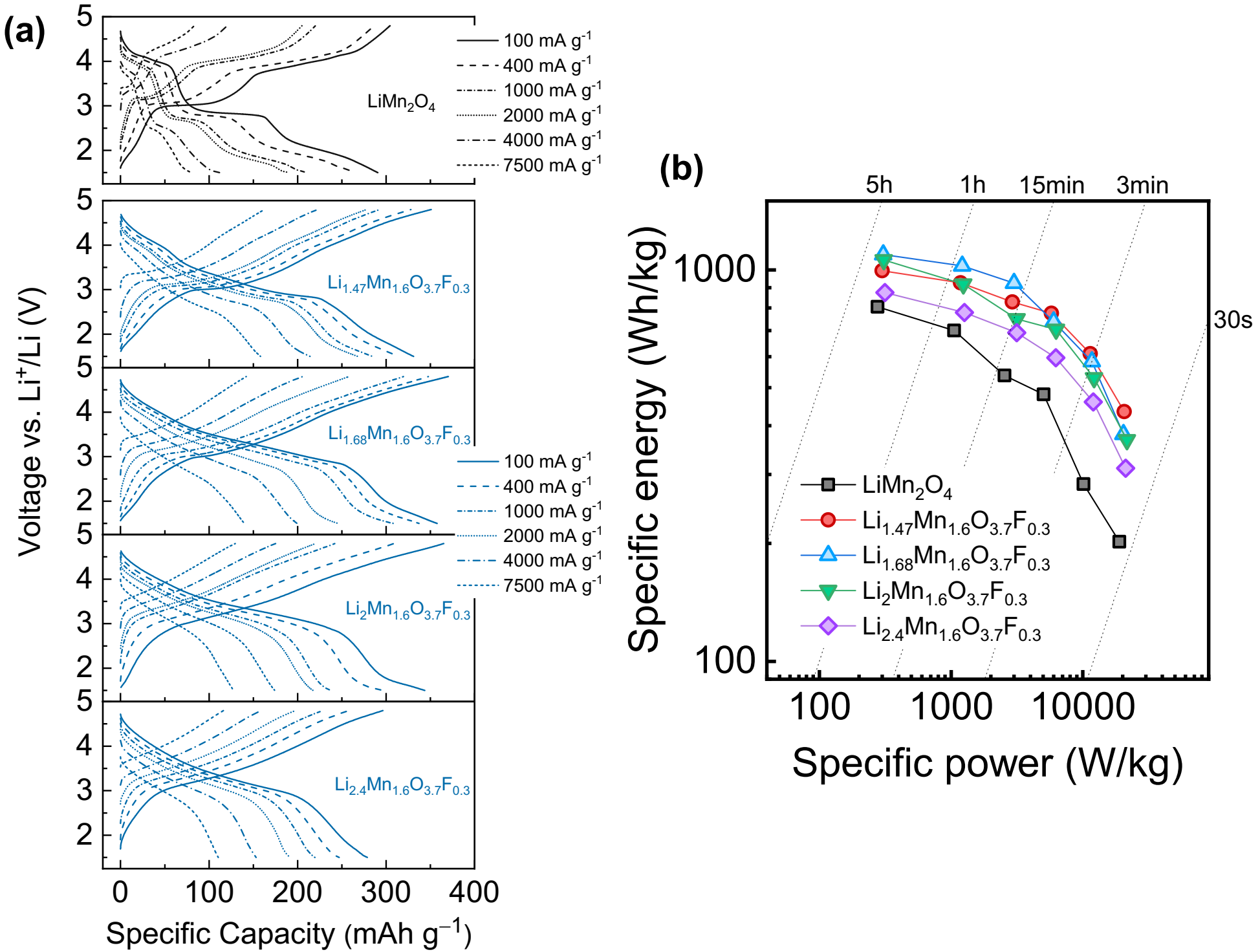
(a)
LiMn2O4
Li1.47Mn1.6O3.7F0.3
Li1.68Mn1.6O3.7F0.3
Li2Mn1.6O3.7F0.3
Li2.4Mn1.6O3.7F0.3
100 mA g-1
400 mA g-1
1000 mA g-1
2000 mA g-1
4000 mA g-1
7500 mA g-1
Voltage vs. Li+/Li (V)
Specific Capacity (mAh g-1)
(b)
5h
1h
15min
3min
30s
Specific energy (Wh/kg)
Specific power (W/kg)

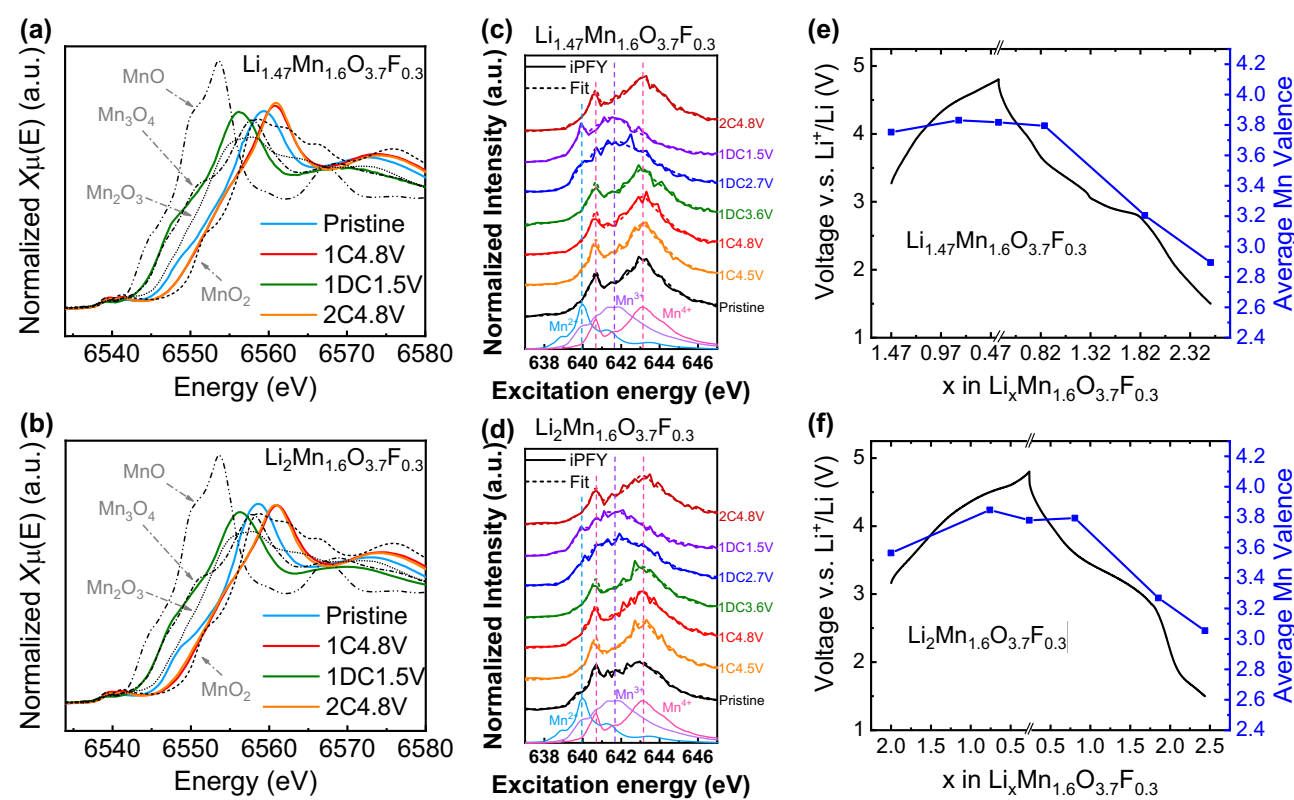
(a)
Li1.47Mn1.6O3.7F0.3
MnO
Mn3O4
Mn2O3
MnO2
Pristine
1C4.8V
1DC1.5V
2C4.8V
Normalized Xμ(E) (a.u.)
Energy (eV)
(b)
Li2Mn1.6O3.7F0.3
(c)
Li1.47Mn1.6O3.7F0.3
iPFY
Fit
2C4.8V
1DC1.5V
1DC2.7V
1DC3.6V
1C4.8V
1C4.5V
Pristine
Mn2+
Mn3+
Mn4+
Normalized Intensity (a.u.)
Excitation energy (eV)
(d)
Li2Mn1.6O3.7F0.3
(e)
Voltage v.s. Li+/Li (V)
Average Mn Valence
x in LixMn1.6O3.7F0.3
(f)

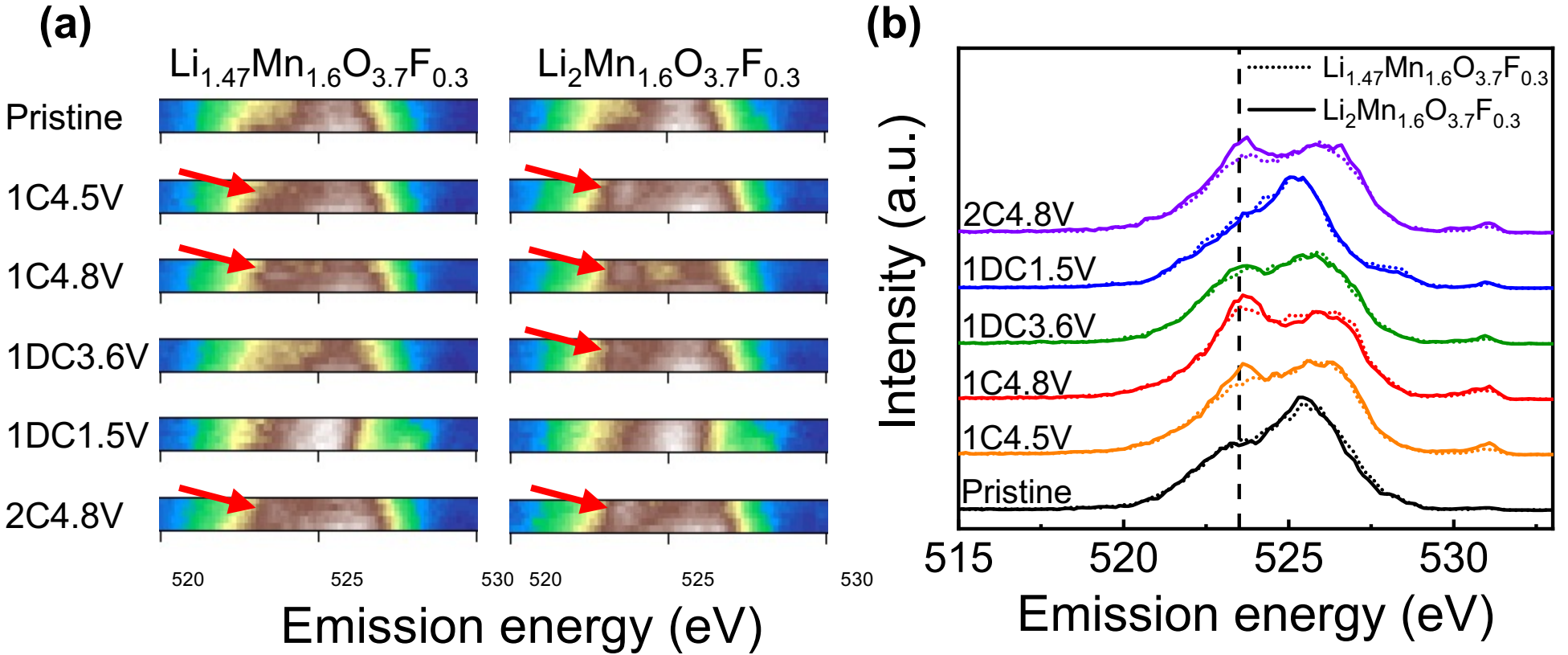
(a)
Li1.47Mn1.6O3.7F0.3
Li2Mn1.6O3.7F0.3
Pristine
1C4.5V
1C4.8V
1DC3.6V
1DC1.5V
2C4.8V
520
525
530
520
525
530
Emission energy (eV)
(b)
Li1.47Mn1.6O3.7F0.3
Li2Mn1.6O3.7F0.3
Intensity (a.u.)
2C4.8V
1DC1.5V
1DC3.6V
1C4.8V
1C4.5V
Pristine
515
520
525
530
Emission energy (eV)

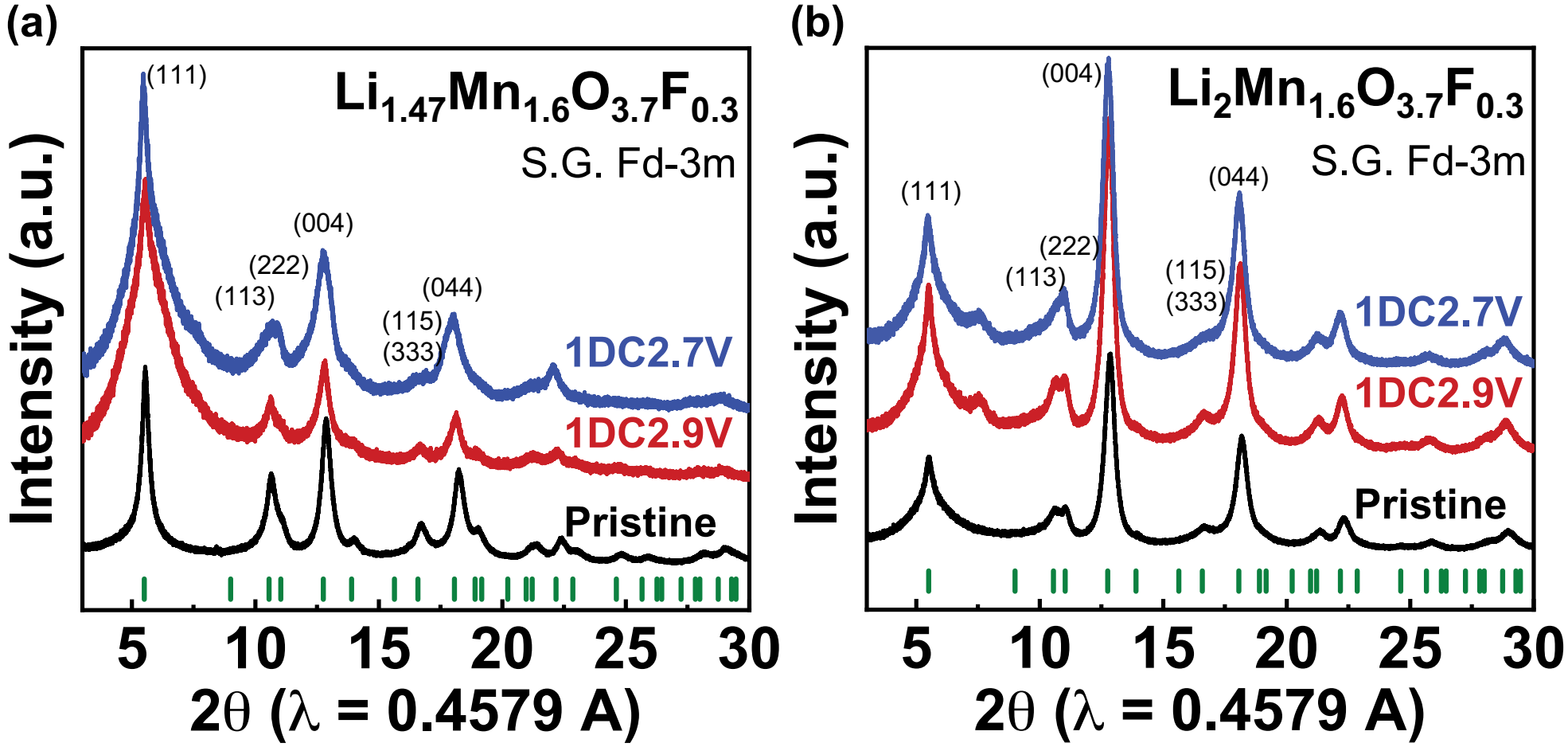
(a)
Li1.47Mn1.6O3.7F0.3
S.G. Fd-3m
(111)
(222)
(004)
(113)
(044)
(115)
(333)
1DC2.7V
1DC2.9V
Pristine
Intensity (a.u.)
5
10
15
20
25
30
2θ (λ = 0.4579 A)
(b)
Li2Mn1.6O3.7F0.3
S.G. Fd-3m
(111)
(004)
(044)
(222)
(113)
(115)
(333)
1DC2.7V
1DC2.9V
Pristine
Intensity (a.u.)
5
10
15
20
25
30
2θ (λ = 0.4579 A)

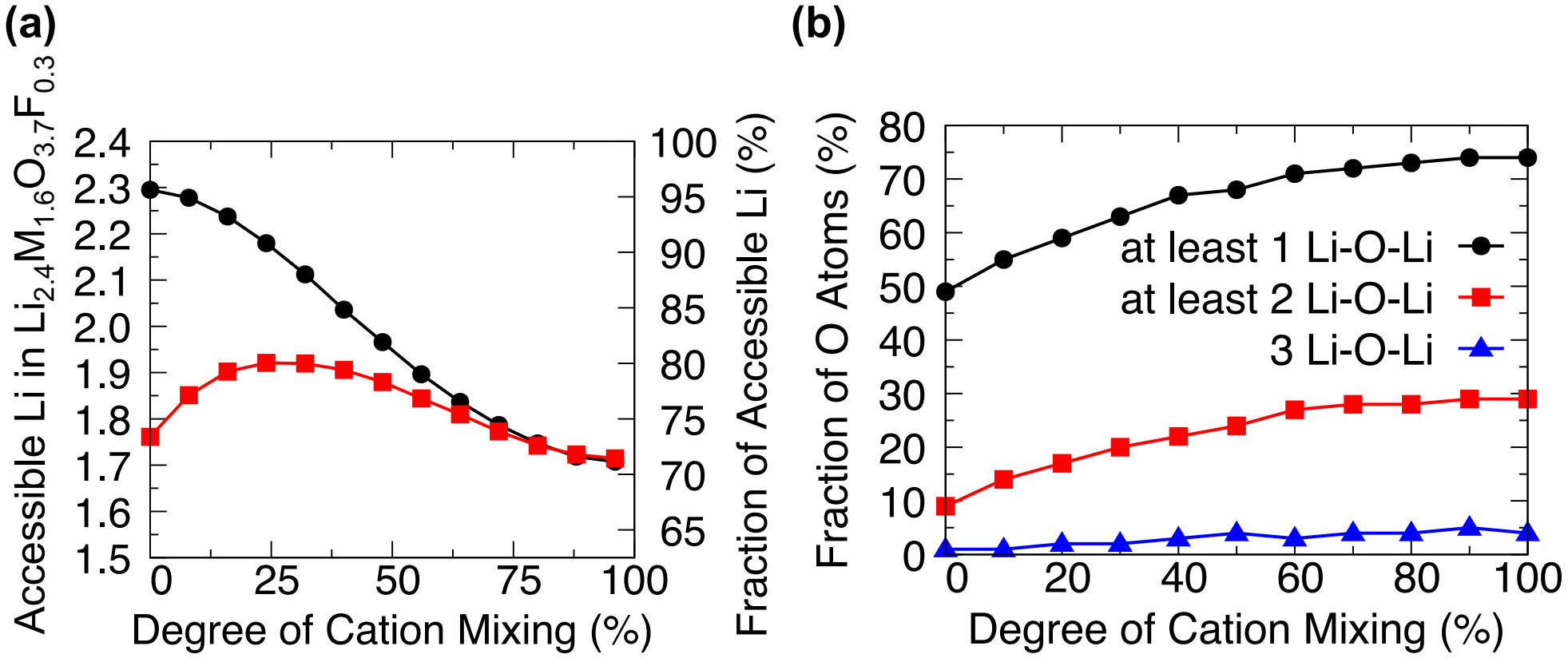
(a)
Accessible Li in $Li_{2.4}M_{1.6}O_{3.7}F_{0.3}$
Fraction of Accessible Li (%)
Degree of Cation Mixing (%)
2.4
2.3
2.2
2.1
2.0
1.9
1.8
1.7
1.6
1.5
100
95
90
85
80
75
70
65
0
25
50
75
100
(b)
Fraction of O Atoms (%)
Degree of Cation Mixing (%)
at least 1 Li-O-Li
at least 2 Li-O-Li
3 Li-O-Li
80
70
60
50
40
30
20
10
0
0
20
40
60
80
100

Fully-ordered Spinel

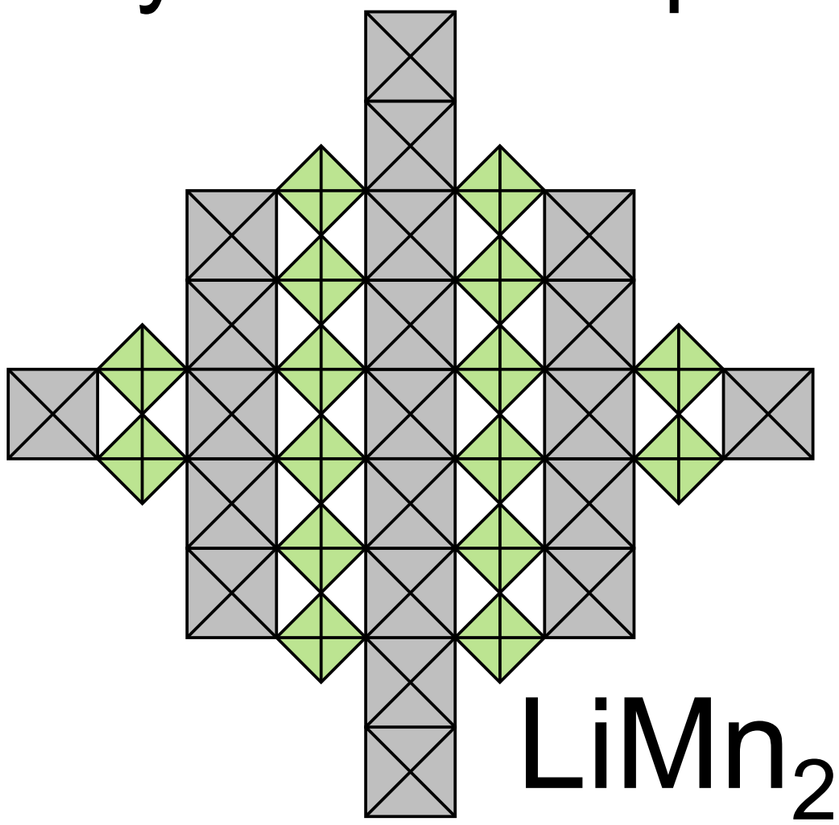

$LiMn_2O_4$

Mn substitution by Li

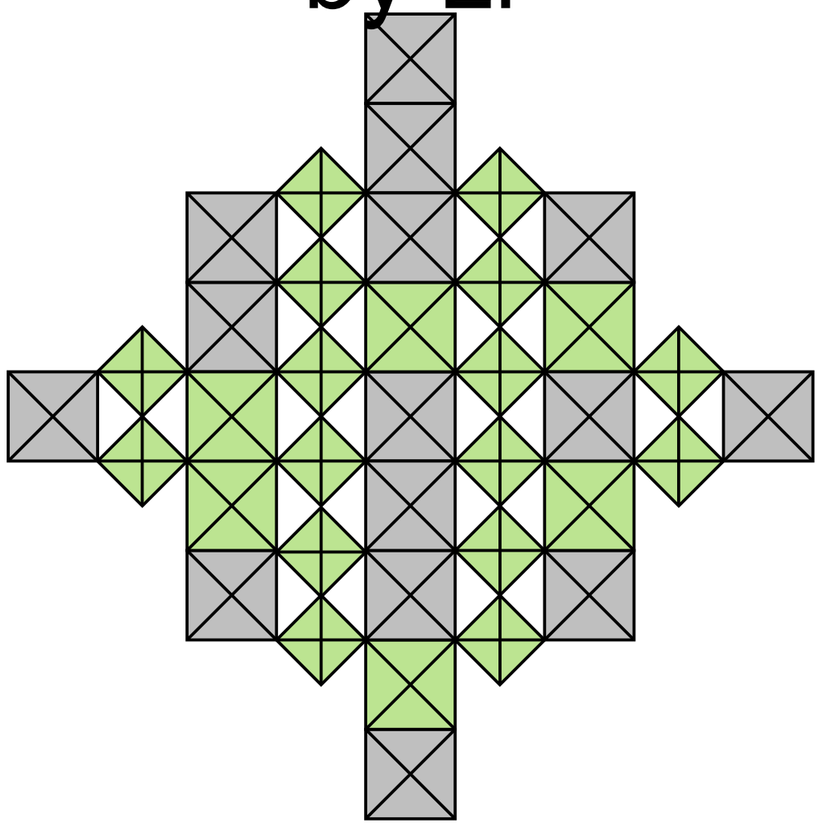

$Li_{1+y}Mn_{2-y}O_4$

Partially-(dis)ordered with Li-excess

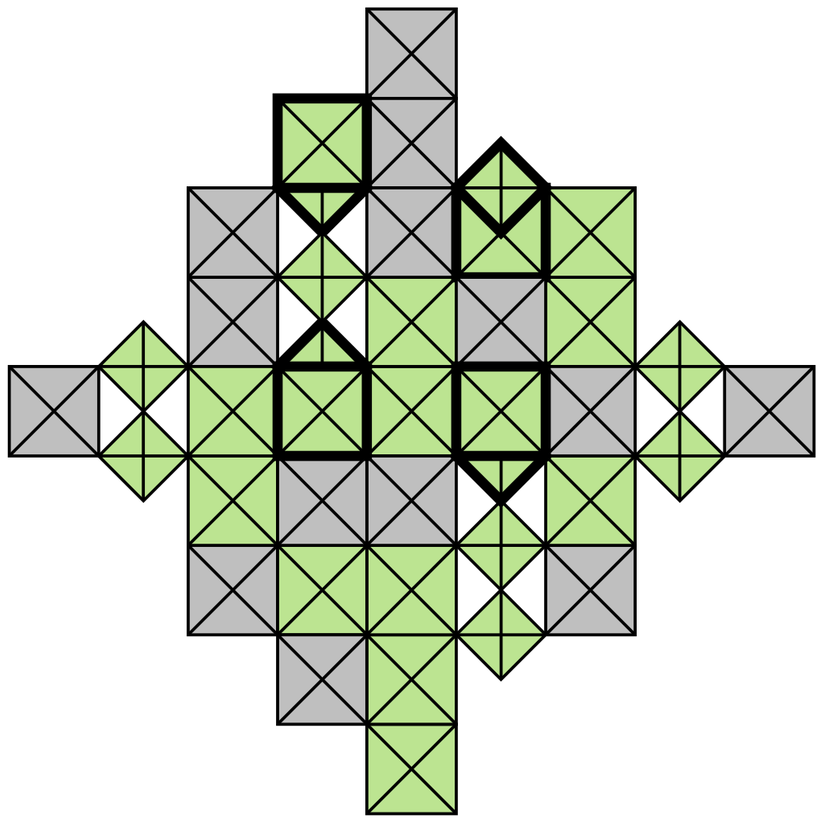

$Li_{1+x+y}Mn_{2-y}(O,F)_4$